Assembly And Tests Of The First Supermodule Of The ALICE Transition Radiation Detector

Diplomarbeit

durchgeführt von
Benjamin Dönigus

unter Anleitung von
Prof. Dr. Peter Braun-Munzinger

April 2007

”..blessed are they that have not seen, and yet have believed.” Joh. 20, 29b

Zusammenfassung

In dieser Arbeit werden der Aufbau und die am ersten Supermodul des ALICE Übergangsstrahlungsdetektors durchgeführten Tests dokumentiert.
Dabei wird auf die Details der Tests der Kammern und insbesondere deren Elektronik eingegangen.
Der Hauptteil der Tests beschäftigt sich mit der Kontroll-Elektronik, die direkt auf den Kammern montiert ist. Die Kammern wurden jeweils zweimal vor ihrem Einbau in das Supermodul getestet, und danach mehfach im Supermodul.
Die komplett bestückten Kammern wurden zweimal getestet bevor sie ins Supermodul eingebaut wurden und dann mehrfach im Supermodul. Das erste Supermodul wurde erfolgreich in Heidelberg zusammengebaut und getestet, und ist jetzt in seiner finalen Position im ALICE Experiment am Large Hadron Collider am CERN eingebaut.
Die Prozeduren für die Inbetriebnahme des Supermoduls als ein Teil des ALICE Experiments haben derzeit begonnen.

SUMMARY

Within this work the assembly of the first supermodule of the ALICE Transition Radiation Detector is described.
Special emphasis is given to the testing of the chambers and its electronics.
The main part of these tests deals with the front end electronics. Fully equipped chambers were checked twice prior to their mounting in the TRD supermodule, and again after the mounting.
The first TRD supermodule has been successfully assembled and checked at Heidelberg and is now installed in its final position at the ALICE experiment at CERN.
First commissioning of the supermodule has started and first data has become available.

Contents

List of Figures

List of Tables

Chapter 1

Introduction

1.1 Introduction

ALICE is the next step in the research of the Quark-Gluon Plasma, with the energies of the LHC (Large Hadron Collider) (5.5 TeV per nucleon pair), the colliding lead ions will create about 20000 particles ($\frac{dN_{ch}}{dy} \approx 2000$) per central event [PPR04; PPR06].
The ALICE experiment is a part of the LHC project at CERN (abbreviation for Conseil Europeen de la Recherch Nucleaire, or European Organization for Nuclear Research). ALICE stands for **A** **L**arge Heavy **I**on **C**ollision **E**xperiment. Under normal conditions the quarks are always glued together forming hadrons. They were once separated, until a few microseconds after the big bang. But in collisions of nuclei at very high energies it is possible to create a so called Quark-Gluon Plasma.

1.2 Nuclear Matter Under Extreme Conditions

Energy and Matter of the universe, even space and time itself, have according to the current cosmologic standard model their origin in a singular initial condition with indefinitely high density and temperature - the big bang - which occured approximately 14 billion years ago. Already after 10^{-35} seconds the temperature dropped dramatically because of the explosive expansion of the universe.
At this stage matter existed as virtually free quarks and gluons, this is known as the Quark-Gluon Plasma (QGP). With continued expansion the temperature continued to drop dramatically. After 10^{-6} seconds the temperature had dropped to 10^{13} K, which corresponds to the so called critical energy density ε_c of approximately 1 GeV/fm^3. While reaching or while dropping below this energy density the phase transition from partonic to hadronic phase happens, in this transition the QGP is condensed into a hot gas consisting of nucleons and other hadrons. As a consequence of this condensation the nucleons could start (about a minute later) to originate the first nuclei of light elements. This lead to the phase, nearly 400000 years later, when nuclei and electrons started to combine and constitute into neutral atoms.
A few million years after the big bang, atoms could clusterise into gas clouds, stars and finally after about one billion years, develop the first galaxies, and start to become the "modern" universe.
Even in today's universe the existence of a Quark-Gluon Plasma is conjectured. Within neutron stars it is expected that the pressure is so high, that the density reaches a multiple of the critical energy concentration and that the usual nuclear matter is dissolved into its constituents to form a QGP.
It is a central concern of heavy ion physics, which creates high energy densities via collisions of nuclei at ultrarelativistic energies, to study quarks and gluons in hadrons under extreme conditions, i.e. high temperatures and densities. It is hoped that at these high energy densities the Quark-Gluon Plasma can be produced and that the phase transition from the Quark-Gluon Plasma to hadrons can be studied as

Fermions	Family	Particle		Mass (MeV/c^2)		El. charge (e)	
Quarks	1	d (down)	u (up)	3 - 7	1.5 - 3	$-\frac{1}{3}$	$\frac{2}{3}$
	2	s (strange)	c (charm)	95	1250	$-\frac{1}{3}$	$\frac{2}{3}$
	3	b (bottom)	t (top)	4200	174200	$-\frac{1}{3}$	$\frac{2}{3}$
Leptons	1	e^- (electron)	ν_e (e-neutrino)	0.5106	$< 2 \times 10^{-6}$	-1	0
	2	μ^- (muon)	ν_μ (μ-neutrino)	105.658	< 0.19	-1	0
	3	τ^- (tauon)	ν_τ (τ-neutrino)	1776.99	< 18.2	-1	0

Table 1.1: Families of fermions in the Standart Model of Particle Physics (Values taken from [PAR06]).

Interaction	couples to	Exchange boson	relative strength	Range (m)
Gravitation	mass	graviton (?)	10^{-38}	∞
Electromagnetic	electrical charge	photon (γ)	10^{-2}	∞
Weak	weak charge	$W^{\pm}$,Z^0	10^{-14}	10^{-18}
Strong	colour charge	gluon (g)	1	10^{-15}

Table 1.2: Overview of the fundamental interactions (taken from [PER00]). The basis of the realtive strength is given by two interacting protons.

well.

1.2.1 Structure And Properties Of Matter

The question of the structure and properties of matter is occupying humanity since thousands of years. In ancient times there was already the idea of an elementary unit for matter, the atom, this idea was further developed mainly through experiments. Today's knowledge of the constituents of matter is described in the following standard model of elementary particles and their interactions.

1.2.2 The Standard Model Of Particles And Their Interaction

According to the standard model of particle physics every form of matter consists of elementary (point-like) particles - quarks and leptons. Quarks and leptons are spin $\frac{1}{2}$ particles, so called fermions, of these there are six kinds. They can be, with ascending mass, divided into three 'families', which are shown in Table 1.1.

For each of these particles an antiparticle exists with equal mass and spin, but opposite electrical charge and colour charge in the case of quarks. The colour charge can assume three values, these can be assigned to the three primary colours red, green and blue or in case of the antiparticles antired, antigreen and antiblue. The colour charge is the charge of the strong force. Together with the weak, the electromagnetic force and the gravity they compose the four fundamental interactions, see Table 1.2. The standard model of particle physics only includes the strong and electroweak forces, where the latter is the unification of the electromagnetic and the weak force, which was formulated within the Glashow-Salam-Weinberg (GSW) theory.

Gravitation on the other hand is excluded, because up to now it is not possible to formulate this, like the other three as a quantum field theory. On a subatomic level gravity is much weaker compared to the other interactions and therefore doesn't have a notable enough influence on the particles.

The fundamental forces are in their individual structure fairly similar through their explanation as the exchange of vector bosons. In the case of the electromagnetic interaction the vector bosons are called

photons, for the weak interaction $W^{\pm}$ and Z^0-bosons, in case of the strong interactions they are called gluons. Gluons have, like the photons a rest mass of zero. Photons are electrically neutral, whereas gluons carry a colour charge and interact with each other. The two main considerable aspects of the strong force are the confinement and the asymptotic freedom, these will be discussed further later on. Even the bosons of the weak interactions carry weak charges, because of this they can interact with each other. As opposed to the other exchange bosons they carry mass ($m_{W^{\pm}} \approx 80$ GeV/c^2, $m_Z \approx 91 GeV/c^2$), because of this the range due to the uncertainty relationship is only limited to 10^{-18} m. Their theoretical prediction was confirmed in 1983 through the experiments UA1 and UA2 at CERN [UA183; UA283].
The large masses of these exchange particles lead to the other main difference between the strong and the weak interactions, which is also expressed in their names, the weak interaction is much weaker than the strong interaction. This leads to the possibility of neglecting higher order processes, like the interaction of exchange bosons among each other.
As already mentioned the six leptons occur as doublets in three families. Each doublet consists of an electrically charged (e, μ, τ) and a neutral lepton (ν_e, ν_μ, ν_τ). Every lepton carries an electrical charge but not a colour charge. Colour charges are only carried by quarks, which also carry electrical and weak charges, and by gluons. As the leptons, the six types of quarks can be arranged in doublets as well.
The six quark eigenstates are called flavours and have the following names: u (up), d (down), s (strange), c (charm), b (bottom) and t (top). The transformation between these flavours can only occur through weak interaction, like the decay of the top quark into a bottom quark and a W^+ or the well known decay of a neutron into a proton, an electron and an electron-antineutrino (at the quark level: $\mathrm{d} \rightarrow \mathrm{u} + e^- + \bar{\nu}_e$).
Under 'normal' conditions, i.e energy concentrations below the critical energy density ($\varepsilon_c \approx 1$ GeV/fm^3), quarks can only be found in colour neutral bound states called hadrons. Such colour singlets can on one hand be built as a $q\bar{q}$ - pair, which is called a meson, or on the other hand as a combination of three quarks (qqq) or three anti quarks ($\bar{q}\bar{q}\bar{q}$) which are a characteristic of so called baryons and antibaryons respectively. These are the simplest hadron constructions, which have already been experimentally proven, but it is possible that multi quark systems exist.
Why quarks can not be found as single free particles will be described in the following paragraph.

1.2.3 Confinement And Asymptotic Freedom

The concept of confinement and asymptotic freedom is formulated within the framework of the quantum field theory of strong interactions - the quantum chromodynamics (QCD). The QCD is a non abelian, i.e non commutative gauge theory also known as Yang-Mills gauge theory which is realized in the colour-SU(3)-algebra. Confinement describes the experimental fact, that quarks only exist in bound colour neutral systems: the hadrons.
This might be connected to the interactions of gluons with each other, this leads to a fall in the potential of the strong interactions. The potential of quarks decreases at short distances r as $1/r$, with this it becomes coulomb like. With longer distances the potential increases linearly and therefore leads to the confinement of quarks to hadrons. With the following (more phenomenological) equation it is possible to express the potential V for $q\bar{q}$ pairs:

$$V = -\frac{4}{3}\frac{\alpha_s}{r} + k\,r,$$

it has the asymptotic behaviour $V(r \rightarrow \infty) \rightarrow \infty$ and $V(r \rightarrow 0) \propto 1/r$. Within this α_s is the coupling constant of the strong interaction, strictly speaking it is not a constant since it depends on the distance. It gets smaller with decreasing distance and increasing momentum transfer Q^2 respectively, since short distances refer to large momentum transfers. According to this the following formula applies:

$$\lim_{Q^2 \to \infty} \alpha_s(Q^2) = 0\,.$$

This is a direct consequence of the QCD and is the so called asymptotic freedom.
The asymptotic freedom describes the fact that quarks can be seen as quasi free particles for large momentum transfers (small α_s value). For the case that $\alpha_s \ll 1$, one can use perturbative calculations as good approximation of the quantum chromodynamic systems. This can be reached experimentally through hard processes. For soft processes, as hadronization, for instance, it is in principle no longer possible to calculate perturbations, since in this case $\alpha_s \approx 1$ applies and therefore terms of a higher order could have a higher influence than terms of the first order. This is often called strong (coupling) QCD.
To find a way around this problem, it is either possible to use phenomenological models or the lattice gauge theory, in which the QCD is treated in an euclidian space-time-lattice, known as Lattice-QCD.

1.2.4 The Quark-Gluon Plasma

The Quark-Gluon Plasma (QGP) is a theoretically predicted state of matter, in which quarks and gluons exist as quasi free particles. To be able to reach this state it is necessary to overcome the binding of the quarks and gluons in the hadrons, the confinement.
According to Lattice-QCD calculations the phase transition between hadronic and partonic phase can be expected to occur at the critical energy density $\varepsilon_c \approx 1$ GeV/fm^3. It is expected that for energy densities above ε_c hadrons loose their individual stability and dissolve into a hot QGP. This state is, in allusion to the inverse process, the confinement, also known as deconfinement.
High energy densities can be reached either through increasing the temperature or the density, to be more precise the baryonic density. Increasing temperature leads to the production of mesons ($q\bar{q}$), which will overlap more and more until they start to dissolve into the QGP once they are above the critical temperature T_c.
Recent Lattice-QCD calculations yield for a baryochemical potential μ_B = 0, i.e the same amount of baryons and antibaryons, a critical temperature of T_c = 151 MeV [AOK06] and 192 MeV [CHE06] respectively. In the second case a baryonic system with a temperature $T \approx 0$ is compressed adiabatically, whereby the baryon concentration is rising. If the critical baryon concentration ρ_c is reached the baryons are begining to overlap, if the baryon concentration continues to rise further a degenerate quark matter system comes into existence.
A schematic phase diagram with strongly interacting matter is as a function of the Temperature T and the baryochemical potential μ_B shown in Fig. 1.1. In Figure 1.1 the possible QCD phases, the phase boundary between hadronic and partonic phase as well as the point of "normal" nuclear matter, indicated by a triangle, can be seen.
Besides the hadronic phase and the Quark-Gluon plasma at a higher baryochemical potential, two other superconductive phases (2SC, CFL) are predicted in which quarks are expected to create a condensate of Cooper pairs [POV06; BUB04; WER04]. Since they are only expected to exist at high baryonic density, e.g. within neutron stars [BAY95; GLE96], these states are unlikely to be produced in heavy ion collisions. In the phase diagram the phase boundary between hadronic phase and QGP is sketched, but the exact spot as well as the order of this phase transition are under current discussion.
Calculations of the phase boundary for areas of high μ_B value are even with the help of the Lattice-QCD extremely difficult and have only been advanced in recent years through new procedures. According to recent model calculations it seems that for higher values of μ_B and low temperatures a phase transition of the first order might exist, which can be marked through the fact that the first derivatives of the free enthalpy $G(T,P)$ are discontinous. In a wide area arround $\mu_B \approx 0$ the phase transition is expected to be a cross over phase transition [AON06] , similar to the melting of butter. But also first and second order

phase transitions are predicted by Lattice-QCD calculations. For second order phase transitions only the second derivatives of the enthalpy are discontinous. The calculations also expect a critical point E where the crossover region ends and the first order phase transition region begins (see for example [FOD04]). To identify such a critical point experimentally would be an important step in the research of QCD phase diagram and this is one of the main goals of the current and future research in the area of heavy ion physics.

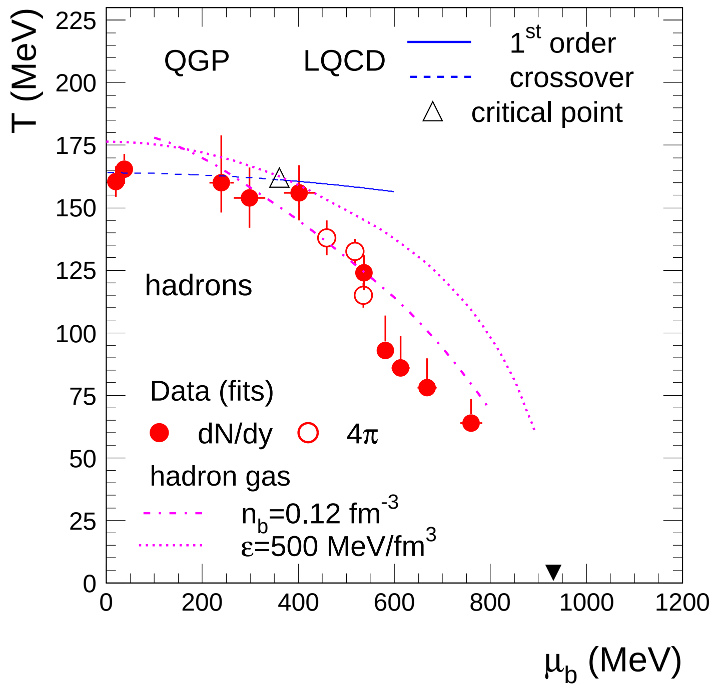

Figure 1.1: Scheme of the phase diagram of strongly interacting matter (taken from [ABS06]).

1.2.5 Relativistic Heavy Ion Collisions

Since the begining of the 1980s heavy ion collisions are performed intensively at different research locations around the world. Here are a few of these locations and their accelerators, they are sorted according to their energy: SIS at GSI (Darmstadt, Germany), AGS at BNL (Brookhaven, USA), SPS at CERN (Geneva, Switzerland) and RHIC at BNL (Brookhaven, USA). Through a multitude of accelerators it is possible to study heavy ion collisions as well as the phase diagram of strongly interacting matter in a wide energy range, namely $2\,\mathrm{GeV} \leq \sqrt{s_{NN}} \leq 200\,\mathrm{GeV}$. In the year 2007 this energy range will be extended through the completion of the LHC at CERN. This will lead to energies up to 5500 GeV per nucleon pair for Pb+Pb collisions. The experiments of heavy ion physics are either fixed target experiments, in which accelerated heavy ions collide with a target, or they are collider experiments in which two beams of heavy ions are accelerated in opposite directions and collide with each other. In both cases we can imagine the colliding nuclei in the center of mass system as lorentz contracted in the direction of movement, e.g. flattened nuclei. The nucleons outside the overlapping area of the colliding nuclei are flying nearly straight on. They are called spectators. The nucleons in

the reaction zone are called wounded nucleons or participants. The energy released through the strong interaction of the participant nucleons (partons) is creating a fireball of hot compressed matter with high particle and energy density.
The expected QGP will exist for a short time ($\approx 10^{-23}$ s) in a small volume (≈ 10 fm radius), and will start to expand because of the high pressure. The expansion will cool the hot fireball, as it did with the early universe, which after cooling down to a critical value, becomes hadronic matter. The hot hadronic gas will expand further, at this stage elastic and inelastic scattering of the hadrons will happen.Once the system has expanded enough, for the inelastic reactions to stop and no changes in the particle multiplicities are ongoing, the so called chemical freeze-out is reached. With ongoing expansion the hadronic gas will get thin enough so that no further elastic collisions happen. This will also stop the changes of the momentum, this is called thermal freeze-out. The decoupled hadrons are measured by a detector setup.
The challenge of proving the existence of a created Quark-Gluon Plasma is to use the indirect information, carried by the particles that can be detected, to come to a conclusion about the phase transition.
Several signatures that are specific for the creation of a QGP are theoretically predicted. A well discussed signature is the J/ψ suppression as a result of the Debye screening. The Debye screening is originally a concept of solid state physics (cp. [ASH76] or [MAR00]) and electrochemistry respectively [DEB23], where the electrical conductivity can be explained by the transition from bound electrons to quasi-free electrons. This is done by introducing a screening by the electrons closer to the nucleus which decreases the potential that an outer electron “sees”. This screening leads to various effects in solids, e.g. one can derive a cut-off frequency from this which leads to a transition from conductor to isolator or vice versa. In the case of the Quark-Gluon Plasma this can be used to explain the behaviour of colour inside the QGP. As mentioned before the colour is the charge of the strong interaction. Therefore one can predict colour screening instead of charge screening. The strength of the screening scales by terms of the temperature. This will lead to the reduction of the probability for c and $\bar{c}$ pairs to form a bound state, i.e. the J/ψ. The formation of QGP leads to the suppression of J/ψs. This can be seen in various experiments with lower energies than the energy the LHC will provide for the ALICE experiment. For these high energies there are predictions for an enhancement of the J/ψs [PBM07]. Within the statistical hadronization model the supression at lower collision energies is explained quite well but as the energies of the LHC are that high a enhancement of the J/ψ production is predicted. The reason for this is the very large amount of particles created at LHC energies, at lower energies the created c and $\bar{c}$ pairs are separated because of the colour screening which reduces the probability of building J/ψs, in the case of LHC there are that many particles created that the colour screening can not reduce the probability of building J/ψ as much as at lower energies. To give evidence of this prediction it is necessary to measure the decay of the J/ψs, which decay either dileptonic (11.87 %±0.12 %) or into hadrons (91.3 %±0.8 % whereas 13.5 %±0.3 % through virtual photons). The dileptonic decay is either into muons (5.93 %±0.06 %) or into electron-positron pairs (5.94 %±0.06 %) [PAR06]. One aim of the ALICE TRD is to identify these electron-positron pairs.
Another signature for the QGP are the emitted dileptons and the emitted direct photons, which are created in the Quark-Gluon Plasma phase. Their yield, angular dependence (with correlation of dilepton-dilepton, photon-photon, dilepton-photon and correlation with jets) and energy are nice criteria to test the theoretical predictions for the QGP state [YAG05].
The suppression of hadronic jets (Jet Quenching) or the reduction of high p_T is caused by the fact that during the collision the quarks and gluons are scattered very hard which normaly leads to partonic jets in which the partons hadronize. In the QGP these jets loose energy due to Gluon-Bremsstrahlung this should decrease the energy and therefore the momentum of the outcoming particles [YAG05].
The enhancement of strangeness, i.e. the rise of particles with the flavour strangeness produced in the QGP, is also predicted as a signature for the creation of a QGP. In the QGP processes like $g+g \rightarrow s+\bar{s}$ or

80%	photons
18%	elektrons/positrons
1.7%	muons
0.3%	hadrons

Table 1.3: Particle composition close to earth surface corresponding to 10^6 produced secondary particles of a shower created by a 10^{15} eV proton [BLÜ00].

$u+\bar{u} \rightarrow s+\bar{s}$ happen, which are faster than in a hadron gas, where processes like $\pi^+ + \pi^- \rightarrow K^+ + K^-$ take place. The reason for this is the lower mass of the s-Quark of $m_s \approx 150\,\mathrm{MeV}/c^2$ compared to the lightest K-Meson with a mass of $m_K \approx 495\,\mathrm{MeV}/c^2$. This should enhance the production of strangeness in nucleus-nucleus collisions compared to proton-proton or proton-nucleus collisions [LAT02; WON94].

1.2.6 Cosmic Rays

Cosmic rays, more precisely the products of their interactions in the atmosphere, can be used to test particle detectors.

We are steadily bombarded by high energy particles from outer space. Approximately one particle hits per second each cm^2 of earth's surface. Cosmic rays were discovered in 1912 by Victor Hess [VÖL00], while he was observing the ionisation of an electrometer which was carried by a balloon. Approximately 1000 meters above sea level the intensity started to rise and at approximately 4000 meters it had almost reached the double intensity. Since 1912 these cosmic rays are studied in detail. Their composition, their energy spectrum, their distribution in space and time are continuously with ever developing experiments observed and theories about their origin have already been suggested. Cosmic radiation is reaching us isotropically from everywhere in space (This and the following referes mainly to [UNS99]. Cosmic radiation has been observed and studied in different heights, deep below the ground, in laboratories on mountaintops, with balloons at heights of up to 40 km, with rockets and satelites. The radiation which enters earth's atmosphere consists of light nuclei, electrons, positrons, photons and neutrinos. It is customary to only call charged particles cosmic radiation. The focus is layed here on ground level cosmic radiation because this is used as the high energy calibration source for our experiment except radioactive sources and test beams at accelerator facilities.

A highly energetic proton, which enters earth's atmosphere, will interact with an oxygen or nitrogen nucleus and will then be lead into a cascade process. A simplified scheme is shown in Figure 1.2. Predominantly there are pions, but also antinucleons, kaons and hyperons will be produced. Now these hadrons can interact with the oxygen and nitrogen nuclei. The unstable ones decay because of the weak interactions, producing electrons, muons, neutrinos and photons. The muons decay, but will due to the time dilatation partially penetrate deep into earth. All in all the high proton energy excites a large number of photons and leptons. A cosmic shower can cover an area of several km^2 in size. With large detector arrays it is possible to detect air showers of up to 10^{20} eV.

Photons on the other hand only excite showers with very small amounts of muons. The main expected ionizing particles in a measured cosmic shower inside the TRD supermodule at the surface are electrons, muons and some hadrons (see Table 1.3). Cosmic showers provide a constant source of energetic particles on earth surface. Later these cosmic showers are used to check the first supermodule of the ALICE Transition Radiation Detector.

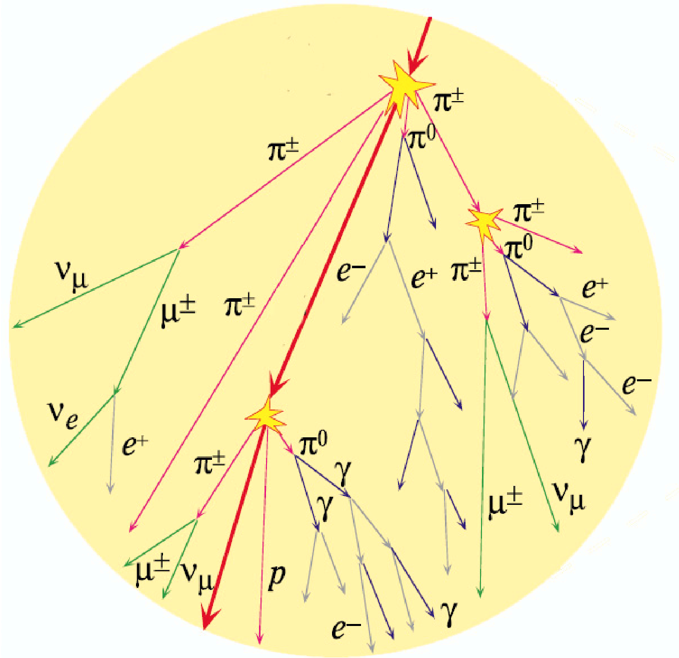

Figure 1.2: Scheme of a cosmic ray shower chain (taken from [BLÜ00]).

1.3 The ALICE Experiment

The ALICE experiment (see Figure 1.3) is divided into many detector systems.
The subdetectors are:

- ITS (**I**nner **T**racking **S**ystem)
  The ITS [ITS99] is composed of silicon detectors of three different types. There are pixel, drift and strip layers. From the beam pipe towards the TPC they surround the beam pipe cylindrically as the first two layers of the silicon pixel detector (SPD) are situated at the radii of 4 cm and 7 cm then there are two layers of the silicon drift detector (SDD) at radii of 15 and 24 cm followed by two layers of the silicon strip detector (SSD) at radii of 39 cm and 44 cm. The ITS is optimized for efficient track finding and high vertex and track impact-parameter resolution. ITS also provides particle identification for the low-p_t region.

- TPC (**T**ime **P**rojection **C**hamber)
  The TPC is the main tracking detector of the experiment. It is the biggest TPC ever built with 95 m^3 gas volume and 527076 pads [REN07]. The gas used is a mixture of Ar (85.7%)/CO_2 (9.5%)/N_2 (4.8%). As the main tracking detector of the experiment it has to provide reconstructed tracks and vertices of the charged particles, therefore it is requested to be able to separate two tracks in a proper way. It also has to perform a charged particle momentum measurement. The particle identification capabilities of the TPC arise from the $\frac{dE}{dx}$ and the momentum measurement. To be able to investigate hard probes, like heavy quarkonia, e.g. charmed and beauty particles but also for high-p_t-jets, the TPC delivers very good momentum resolution as well as good spatial resolution up to high momenta ($p_t = 100$ GeV/c) [TPC00].

- TRD (**T**ransition **R**adiation **D**etector)
  The TRD will be described in a special chapter, Sec. 2.2.

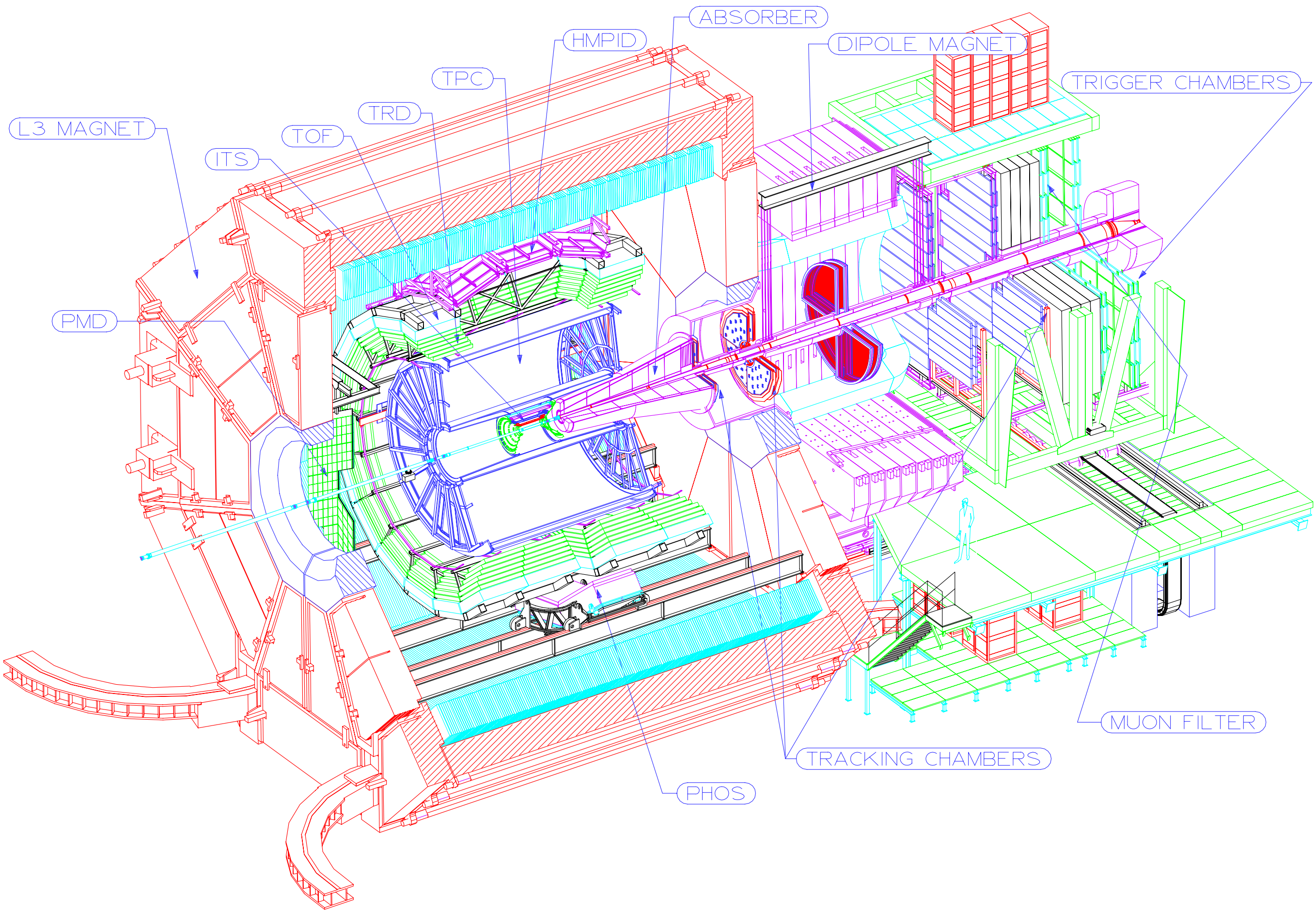

Figure 1.3: Schematic view of the ALICE experiment.

- TOF (**T**ime **O**f **F**light)
  The TOF detector of ALICE [TOF02] is built for particle identification in the region where ITS and TPC are no longer accurate enough, it is also the last part of the tracking chain. The TOF is built of multigap resistive plate chambers. A uniform electric field is produced inside the gas chamber, which is divided into ten gaps. They are small in order to increase the timing capabilties of the detector. The TOF consists of 18 supermodules placed inside the space frame above the TRD supermodules.

- HMPID (**H**igh **M**omentum **P**article **I**dentification **D**etector)
  The HMPID [HMP98] is mainly built to identify charged particles with momenta above $p_t > 1$ GeV/c. The HMPID is using Cherenkov radiation which is emitted when a particle has a larger speed than light in a medium. The detection method of the HMPID is called RICH (Ring Imaging CHerenkov counter). The Cherenkov light is produced in a radiator filled with liquid C_6F_{14}. A multiwire proportional chamber detects the light and the particle which created the Cherenkov light. The pads used are covered by CsI which is a photosensitive material, this is used to detected the Cherenkov light (in an optimal case a ring corresponding to the Cherenkov cone).

- MUON Spectrometer
  The muon detector or dimuon detector, will be used to detect muons respectively muon pairs.

They are mainly produced by decays of heavy quarkonia (i.e. J/ψ, ψ', Υ, Υ' and Υ''). To detect only the muons, other particles (e.g. hadrons and photons) have to be stopped by a big front absorber built of several layers of different materials. After the absorber there are several muon tracking chambers (cathode strip chambers CSCs), surrounded by the dipole magnet. The magnet is needed to separate postive and negative charged muons. After the tracking chambers a muon filter is placed to absorb the low energy muons and background. This is followed by trigger chambers, build as resistive plate chambers. These can provide a muon trigger but also can be used in combination with the TRD as a muon/electron coincidence trigger.

- PHOS (**PHO**ton **S**pectrometer)
  The Photon Spectrometer [PHO99] is a high resolution electromagnetic spectrometer which will provide photon identification as well as neutral pions identification. It consists of 17280 channels of lead-tungstate crystals ($PbWO_4$ or PWO) and is sitting on the bottom of the ALICE experiment. It will identify photons, discriminate direct photons from decay photons and perform momentum measurements over a wide dynamic range with high energy and spatial resolution.

- EMCAL (**E**lectro**M**agnetic **CAL**orimeter)
  The EMCAL [EMC06] is an electromagnetic spectrometer with a design similar to the calorimeter used at the PHENIX experiment at RHIC. The EMCAL will focus on the jet and high-p_T photon physics but it will also maintain hadron ID capability. It is the newest proposed subdetector of ALICE and still in a research and development state. The technology used is a layered Pb-scintillator sampling calorimeter with a longitudinal pitch of 1.6 mm Pb and 1.6 mm scintillator. The readout will be done with scintillators which collect the light via wavelength-shifting fibres running through the Pb-scintillator tiles perpendicular to the front surface.

- FMD (**F**orward **M**ultiplicity **D**etector)
  The main aim of the silicon strip Forward Multiplicity Detector [FOR04] is to give offline information about the charged particle multiplicity. It can be used as a high multiplicity trigger at an early stage in the trigger chain (Level 0) or when the trigger decission is at further stage (Level 1).

- V0
  The V0 detector [FOR04] has to provide a minimum bias trigger for the central barrel detectors (ITS, TPC). It also has to provide centrality triggers in lead-lead collisions. It can be used as a centrality indicator in multiple roles. It can also be used for a validation signal for the muon trigger to filter background in pp collisions. The V0 is a small-angle detector consisting of two arrays of scintillator counters.

- T0
  The T0 detector [FOR04] has to generate time related signals for the whole ALICE trigger chain. It has to produce the T0 signal for the TOF detector, which corresponds to the real time of the collision (plus a fixed time delay). It can be used to measure the vertex position (with a precision of $\pm$ 1.5 cm) for each interaction and to provide a L0 trigger when the position is within a given range. It also has to provide an early 'wake-up' signal for the TRD, which has to come prior to the L0 level. Since the T0 detector generates the earliest L0 trigger signals, they must be very fast. The dead time of the detector has to be less than 25 ns which corresponds to the bunch-crossing period in pp collisions. The T0 consists of two arrays of 12 Cherenkov radiators optically coupled to photo-multiplier tubes.

- PMD (**P**hoton **M**ultiplicity **D**etector)
  The PMD [PMD99] is as preshower detector build as honeycomb gas proportional counters with

extended cathodes. It will measure the multiplicity and spatial distribution of photons on an event-by-event basis, which provides the possibility to study event shapes and fluctuations in the forward region where large particle densities impose very severe constraints. Using the preshower signal the PMD will provide estimates of transverse electromagnetic energy.

- ZDC (**Z**ero **D**egree **C**alorimeter)
  The main task of the ALICE ZDC [ZDC99] is to detect the spectators, which are as mentioned before nucleons which are not part of the reaction, giving a direct measure of the centrality of the event. This can be used for example as a L0 rejection criterion. The ZDC can also be used as a luminosity monitor. The used technique for the ZDC is quartz fibre calorimetry.

The ALICE experiment also consists of several groups which provide the utilities for data taking and processing (DAQ), guarantee communication between the data acquisition part and the detectors as the Experimental Control System (ECS) and the controlling of the detectors as the Detector Control System (DCS), and they supply the detectors with the needed materials like gas, electricity (low and high voltage) and cooling.

Chapter 2

ALICE TRD

2.1 Transition Radiation

The transition radiation (TR) was found experimentally in 1959 in an optical region by Goldsmith and Jelley [GOJ59]. It was already predicted in 1946 by Ginzburg and Frank [GIN46] but the number of created quanta is very small, which might be a reason for the late experimental verification. The transition radiation is emitted when ultrarelativistic particles pass through borders between media with different dielectric properties. To increase the number of emitted photons one has to increase the number of borders passed. That can be done for example with thin layers of two materials with different refractive indices, which are put in layers one after the other, e.g. foils. Another possible solution for a radiator for TR is taking foams, typically one material in the foam is air. For the ALICE TRD different types of radiators were tested [AND06]. The final radiator is a sandwich made of foam and fiber materials. This structure provides mechanical rigidity against deformations caused by gas overpressure.
The emission of transition radiation is related to the dielectric properties of the materials crossed by the charged particle. Therefore the electrodynamics of the emission is described by using the plasma frequency ω_p of the given material (the theory of transiton radiation can be found in more detail for instance in [JAC99], [PAR06] or [DOL93]).

$$\omega_\mathrm{p} = \sqrt{\frac{4\pi\alpha n_e}{m_e}} = 28.8\sqrt{\rho\frac{Z}{A}}\,\mathrm{eV}\,,$$

where α is the fine structure constant ($\alpha = \frac{1}{137}$), n_e is the electron density, m_e is the electron mass, ρ is density given in $\frac{\mathrm{g}}{\mathrm{cm}^3}$, Z is the atomic number and A is the atomic mass.
The emitted intensity I of the photons created by charged particles crossing the boundary between the two media described by their plasma frequency is given by:

$$I = \frac{\alpha\hbar^2}{3}\frac{(\omega_{\mathrm{p}1} - \omega_{\mathrm{p}2})^2}{\omega_{\mathrm{p}1} + \omega_{\mathrm{p}2}}\gamma,$$

where γ is the Lorentz factor $\gamma = \frac{1}{\sqrt{1-(\frac{v}{c})^2}} = \frac{E}{mc^2}$ and $\hbar = 6.58211915 \times 10^{-22}\,\mathrm{MeVs}$ is the reduced Planck constant. The differential power spectrum radiated by a charged particle passing through a boundary of two dielectric media can be written like the following expression [ART75]:

$$\frac{\mathrm{d}^2W}{\mathrm{d}\omega\Omega} = \frac{\alpha}{\pi^2}\left(\frac{\Theta}{\gamma^{-2}+\Theta^2+\xi_1^2} - \frac{\Theta}{\gamma^{-2}+\Theta^2+\xi_2^2}\right)^2,$$

whereby $\xi_1^2 = \frac{\omega_{P1}^2}{\omega^2} = 1 - \varepsilon_1(\omega)$, $\xi_2^2 = \frac{\omega_{P2}^2}{\omega^2} = 1 - \varepsilon_2(\omega)$ and Θ is the emission angle. This formula applies for $\gamma >> 1$, ξ_1 and $\xi_2 << 1$ and $\theta << 1$. Integration of the energy spectrum leads to

$$W = \frac{\alpha\hbar}{\pi} \frac{(\omega_1 - \omega_2)^2}{\omega_1 + \omega_2} \gamma.$$

The linearity of the resulting equation shows how to distinguish between the different particles corresponding to their Lorentz factor. Electrons are the only particles which emit transition radiation in a momentum range from 1 to 100 GeV/c. Since $\Theta << 1$, $\sin\Theta \approx \Theta$ the emission angle for most of the emitted photons can be estimated by

$$\Theta \approx \frac{1}{\gamma}.$$

To detect the transition radiation, which in case of the ALICE TRD is X-ray radiation (up to 40-50 keV) [BUS04], typically drift chambers are used. Therefore the used gas has to have a high number of electrons (high Z) to increase the probabilty of absorption.

2.2 Detector Design Of The ALICE TRD

A comprehensive summary of the design, construction and performance of the ALICE TRD is given in the Technical Design Report (TDR) [TRD99]. This part of the thesis will only summarize some basic facts and some specialities which have changed since the TDR. The TRD parameters are shown in Table 2.1. The main aim of the ALICE TRD is to identify electrons with momenta above 1 GeV/c, where the TPC is no longer efficient in pion rejection using dE/dx. It will also be used as an efficient trigger for high-transverse-momentum electrons. This trigger will increase the recorded Υ yields as well as the high-p_T J/ψs [TRD99],[PPR04].

The ALICE TRD is built of 18 supermodules mounted in radial direction between the TPC and the 18 TOF supermodules (Figure 2.1). Each TRD supermodule consists of 30 multi-wire proportional drift chambers. In total the TRD consists of 540 drift chambers or readout chambers (ROCs). Each readout chamber consists of a radiator of 4.8 cm thickness followed by a multi-wire proportional drift chamber. The signal induced on cathode pads is read out. Therefore each readout chamber is covered by its readout electronics. Each chamber has 144 pads in the direction of the amplification wires, $r\varphi$, and either 12 (C0 chambers) or 16 (C1 chambers) pad rows in the z direction. The pads have a typical area of 6–7 cm^2 ($\approx 0.75 \times 8\,\text{cm}^2$) and cover a total active area of about 736 m^2 with 1.16×10^6 readout channels. The induced signal at the cathode pad plane is sampled in time steps, called time bins, corresponding to 100 ns each.
The principle of the ALICE TRD is sketched in Figure 2.2. The left part shows a projection in the plane perpendicular to the wires. Electrons produced by ionization energy loss ($\mathrm{d}E/\mathrm{d}x$) and by TR absorption move along the field lines towards the anode wires. The right panel shows a projection in the bending plane of the ALICE magnetic field. In this direction the cathode plane is segmented into pads from 0.635 to 0.785 cm width. The little insert in the right part shows, for a measured electron track, the distribution of pulse height over pads and time bins spanning the drift region of an electron. For pions only ionization clusters are produced in the gas while for electrons TR energy is deposited on top, see Figure 2.3. The free electrons produced by ionization and transition radiation absorption drift towards the anode wires where they create avalanches. The position of the hit is reconstructed by charge sharing on adjacent cathode pads, enabling precise tracking in the bending plane.
Each supermodule is divided in radial direction in 6 layers to increase the quality of the electron identification, and 5 stacks in z direction (the layers are counted from 0 to 5, the stacks from 0 to 4).

Table 2.1: Synopsis of TRD parameters (derived from [PPR04]).

Pseudo-rapidity coverage	$-0.9 < \eta < 0.9$
Azimuthal coverage	2π
Radial position	$2.9 < r < 3.7$ m
Length	up to 7.0 m
Azimuthal segmentation	18-fold
Radial segmentation	6 layers
Longitudinal segmentation	5-fold
Total number of modules	540
Largest module	117×147 cm^2
Active detector area	736 m^2
Radiator	fibres/foam sandwich, 4.8 cm per layer
Radial detector thickness	$X/X_0 = 15\%$
Module segmentation in φ	144
Module segmentation in z	12–16
Typical pad size	$0.7 \times 8.8 = 6.2$ cm^2
Number of pads	1.16×10^6
Detector gas	Xe/CO_2 (85%/15%)
Gas volume	27.2 m^3
Depth of drift region	3 cm
Depth of amplification region	0.7 cm
Nominal magnetic field	0.4 T
Drift field	0.7 kV/cm
Drift velocity	1.5 cm/μs
Lorentz angle	8°
Number of readout channels (pads)	1181952
Time samples in r (drift)	30
Number of readout pixels (used ADC channels)	1378944
ADC	10 bit, 10 MHz
Number of multi-chip modules	70 848
Number of readout boards	4 104
Pad occupancy for $dN_{ch}/d\eta = 8000$	34%
Pad occupancy in pp	2×10^{-4}
Space-point resolution at 1 GeV/c in $r\varphi$	400 (600) μm for $dN_{ch}/d\eta = 2000$ ($dN_{ch}/d\eta = 8000$)
in z	2 mm (offline)
Momentum resolution	$\delta p/p = 2.5\% \oplus 0.5\%(0.8\%)p$ for $dN_{ch}/d\eta = 2000$ ($dN_{ch}/d\eta = 8000$)
Pion suppression at 90% electron efficiency and $p \geq 3$ GeV/c	better than 100
Event size for $dN_{ch}/d\eta = 8000$	11 MB
Event size for pp	6 kB
Trigger rate limits for minimum-bias events	100 kHz
Trigger rate limits for pp	100 kHz

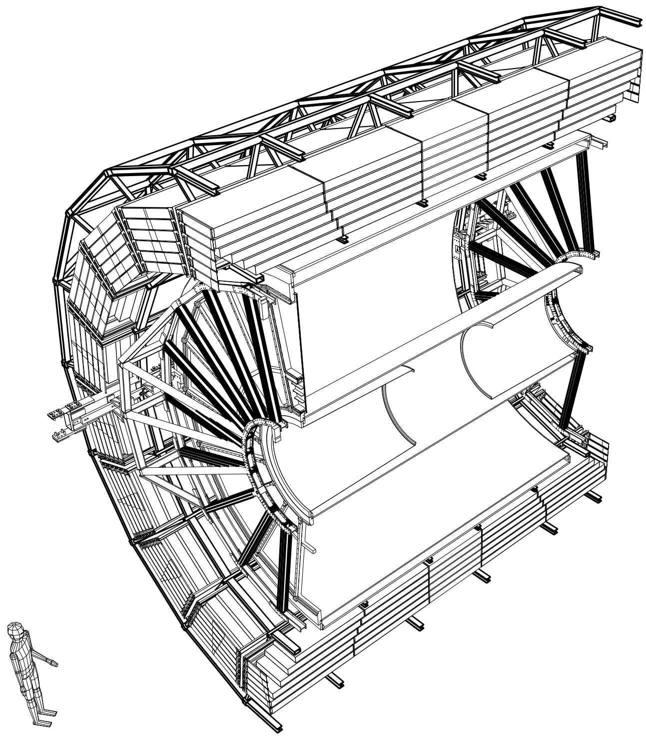

Figure 2.1: Cut through the ALICE TRD with the TPC inside. One can see the layer and stack structure of the TRD.

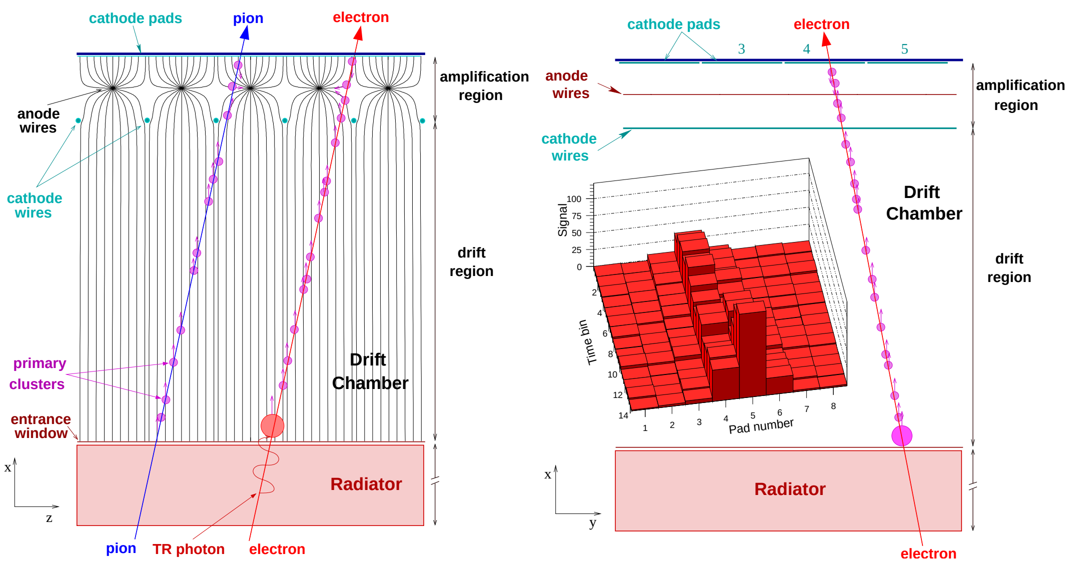

Figure 2.2: Illustration of the principle of the ALICE TRD.

2.2.1 Gas And Field Properties

The gas mixture in the readout chambers is Xe/CO_2 (85%/15%), Xenon is taken to provide efficient transition radiation photon absorption because of the high Z, CO_2 is used as quenching gas. Each readout

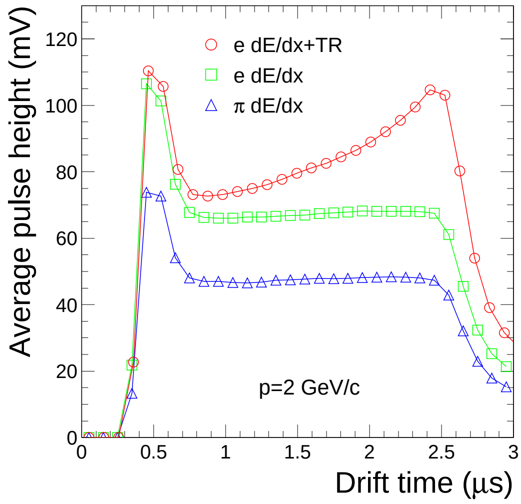

Figure 2.3: Pulse height versus drift time. The difference of the particles without emitting transition radiation and with emitted transition radiation can clearly be seen as larger average signals at larger drift times due to absorbed transition radiation. The different pulse heights indicates the difference of the ionization enrgy of pions and electrons.

chamber consists of a drift region of 3.0 cm separated by cathode wires from an amplification region of 0.7 cm. For this gas mixture the maximum drift time is about 2.0 μs, requiring a drift velocity of 1.5 cm/μs. Each timebin corresponds to 1.5 mm drift region. The nominal drift velocity is reached with an electric field of 0.7 kV/cm. In this gas mixture a minimum ionising particle liberates on the average 275 electrons/cm. The gas gain is of the order of 5×10^3. The fields are created using +1.65 kV for the anode wire plane and -2.1 kV for the drift electrodes, provided by ISEG high voltage modules. In the final mode of operation the voltage will be provided through a setup (High Voltage Distribution System) developed in Athens. It will multiply the HV created by the ISEG modules and provide it to the supermodules.

2.2.2 Low Voltage

For the operation of the frontend electronics (FEE) and the control electronics (DCS) low voltage is needed. The low voltage is provided to the loads via long copper power bus bars mounted on the side of the supermodule. For the electronics four voltages and the corresponding grounds are needed:

1. 3.3 V Digital, for the TRAP part of the multi chip module (see Section 3.1.1),
2. 1.8 V Digital, also for the TRAP part,
3. 3.3 V Analog, for the PASA, and
4. 1.8 V Analog, for the ADCs.

The voltages are given by the Wiener power supplies (see Figure 5.3) which are water-cooled floating power supplies. Since there are losses inside the power bus bars and the patch panel, the voltage given at the power supplies has to be above that expected at the readout boards. The power to the DCS boards (3.3 V and 1.8 V), which control the frontend electronics of each readout chamber is also given by the

Wiener power supplies but provided through a device called PDB (**P**ower **D**istribution **B**ox) [STE07]. To be precise the PDB only delivers around 4 V to the DCS board, and the voltage regulators produce the 3.3 V and 1.8 V on the DCS board.

2.2.3 Cooling

The electrical heat produced by the frontend electronics is compensated by liquid cooling. Cooling pipes with a special geometry are glued onto the multiple chip modules which are the main processing regions and for this reason the hottest part of the readout boards. The cooling is done through cooling bus bars for each layer connected to the cooling pipes on each readout chamber. The cooling bus bars are connected via tubes to each other so that only one inlet and one outlet for the cooling is needed for one supermodule. The cooling is done with underpressure, to avoid spills in case of accidental leaks.

Chapter 3

Front End Electronics

3.1 Introduction

3.1.1 Multiple Chip Modules

The front end electronics of the TRD is based on the multi chip module (MCM), see Figure 3.1. It consists of two chips. The TRAP (**TRA**cklet **P**rocessor) chip and the PASA. The PASA is the preamplifier/shaper chip which provides the detector signal in an amplified and shaped form to the TRAP chip. An overview of the electronics chain can be found in Figure 3.2.

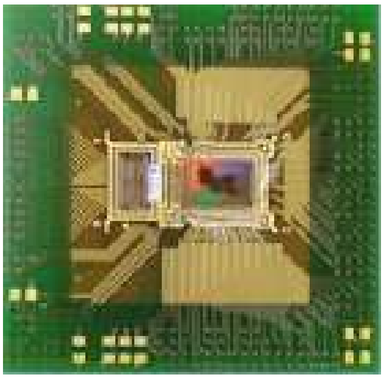

Figure 3.1: Picture of a bare MCM and a picture of a MCM as mounted on the readout boards.

3.1.2 PASA

The PASA can be divided into several sub-circuits. The main purpose of the Charge Sensitive Amplifier (CSA) is to integrate the short current pulse deposited by a particle on the pad for energy measurement [SOL07]. To preserve this energy and at the same time fulfil the requirement given in table 3.1, was the following preamplifier shaper circuit topology developed.
A block diagram of the preamplifier shaper chain is shown in Fig. 3.3. Each channel of the 18 channel version consist of a preamplifier, a pole-zero network, two second order bridged-T filters and two non-inverting stages each providing a fixed gain of 2. A Common-Mode Feed Back circuit (CMFB) is included to assure common-mode stability. In addition and not shown in the block diagram is the self-adaptive bias network, the internal bias network and the threshold referenced self-biased network.
The main functionalities of the PASA are:

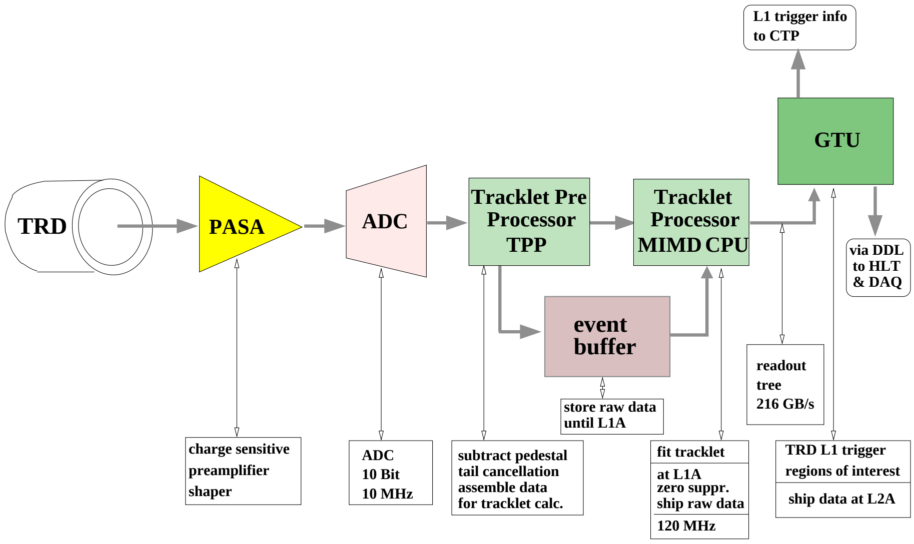

Figure 3.2: Block diagram of the TRD front-end electronics (taken from [TRD99]).

Parameters	Specification	Tested
Noise (25 pF)	< 1000 e	850 e
Shaping time (ns)	120	≈ 120
Int. non-linearity	$< 1\,\%$	0.5 %
Conv. gain $\left(\frac{\text{mV}}{\text{fC}}\right)$	12	≈ 12
Power $\left(\frac{\text{mV}}{\text{fC}}\right)$	< 20	≈ 14

Table 3.1: Main specifications of the ALICE TRD PASA (taken from [SOL04]).

1. Integrate the charge deposited by a particle on the pad over the feedback capacitor C_{fb}. This will in the ideal case give a voltage at the output of the preamplifier of: $V_{\text{out}} = \frac{Q}{C_{\text{fb}}}$, where Q is the deposited charge. To avoid saturation of the preamplifier, is the integrated signal over the feedback capacitor C_{fb} decharged through a feedback transistor with an impedance of $10\,\text{M}\Omega$. This relatively huge value is a compromise between noise and pulse rate.

2. The long and finite decay time of the preamplifier signals generates undershoot at the amplifier output. This is compensated by the pole-zero cancellation that is done by the inclusion of the transistor M_f in parallel with the capacitance C_f.

3. In order to filter as much noise as possible from the signal, to provide a quick return to the baseline, to allow high counting rate and to meet the gain requirement are the CSA and the pole-zero network followed by two brigded-T filter stages that in total gives a CR-RC^4 semi-Gaussian shape.

4. After the signal is shaped and optimized for noise, the differential signal is split in two around the common-mode voltage (900mV). The output DC-level is internally set by $V_{\text{ref+}}$(1.4V) and $V_{\text{ref}-}$(0.4V), giving a DC level at the output of 0.4V ($V_{\text{out+}}$) and 1.4V ($V_{\text{out}-}$), respectively.

This shows an optimised signal that is sent to the ADC for further processing.

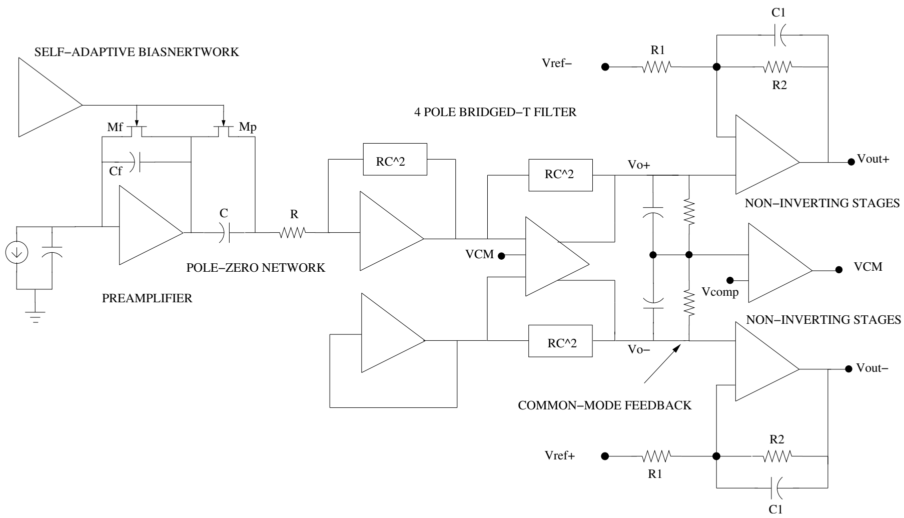

Figure 3.3: Block diagram of the ALICE TRD PASA [SOL07].

3.1.3 TRAP

The TRAP chip is the main digital part of the MCM. Its structure is shown in Figure 3.5. It receives the analog preamplified and shaped signal and digitizes it. Therefore the TRAP chip has 21 ADC channels. The main aim however is the processing of the digitized data to tracklets. Therefore the TRAP chip has 4 CPUs [ANG06], each with:

- IMEM (IMM), which is the instruction memory (4k x 24 bits + hamming), they are used to buffer the instructions which come through the Slow Control Serial Network (SCSN).
- DMEM (DMM), this is the common data memory (1k x 32 bits + hamming), it can be used as a lookup table, for support calculations or for corrections.
- DBANK (DDD), this is the common data bank memory (256 x 32 bits). It can be used as a buffer for incoming and outgoing messages from the SCSN. It should not be used to manipulate tracklets because of its slowness and the missing hamming properties.

The TRAP is accessible directly through the SCSN interface. The used ADCs are full custom 0.18 μm design of a 10 bit 10 MHz differential ADC with a power consumption of about 5 mW per channel. It is followed by a digital filter in order to compensate tails of the pulses due to slow ion drift and tails from the electronics (overall known as the time response function). Without such a filter significant distortions in the position measurement would be incurred depending on the history of the signals. These position measurements are used to reconstruct the short track pieces (tracklets) inside the drift region. The output of the digital filters is directly fed into the tracklet pre-processor. Here, all relevant sums are calculated which are subsequently used by the tracklet processor in order to calculate the position and inclination of tracklets. Up to four candidate tracklets per MCM are shipped to the Global Tracking Unit (GTU), where tracklets from the individual layers are combined and matching cuts as well as momentum cuts and more involved cuts (such as cuts on the invariant mass of pairs) can be applied. The GTU will be implemented in FPGAs close to the Central Trigger Processor (CTP). The trigger decision of the TRD is sent to the CTP 6 μs after the interaction.
The TRAP has a GSM (**G**lobal **S**tate **M**achine) which defines the actual state of the TRAP, see Table 3.2 and Figure 3.4. The states correspond to the several stages in the trigger chain. It can be used to identify bad MCMs, since one is in a certain state and all others in another state, e.g. wait_pre.

State	Binary code	Hex code	State name
Low power state	0000	0	low_powr
Test mode	0001	1	test_chk
Wait for pretrigger	0011	3	wait_pre
Preprocessor is running	0111	7	preproc
CPUs proceed the tracklets	1111	F	tr_proc
Send the tracklet information	1110	E	tr_send
Wait for the L1 accept	1100	C	wait_L1
CPUs make zero suppression	1000	8	zero_sp
Full readout	1001	9	full_rd
Clear state, prepare for next event	1011	B	clear_st

Table 3.2: The global states of the TRAP.

3.1.4 Readout Boards

The MCMs are situated on the readout boards (ROBs). The readout boards are 6-layer PCB boards, which provide the connection of the MCMs in the readout chain but also to the SCSN rings to control the MCMs. There are 7 different types of readout boards for the 8 positions on the chamber. The readout boards are connected in two different ways: The readout way (first in Φ then in z-direction) and the SCSN way (in Φ direction). The ROBs have to provide the structure to send and receive all types of signals, like pre-trigger/trigger, clock, power, shutdown, control and the produced data. The connection between ROBs is done using custom cables (cable boards). They connect the readout boards in the different directions on the chamber. There are different kinds of connectors for the different connections. The function is coded by colour, e.g. green connectors are used for SCSN connections in φ-direction, red for distributing the clock and pretrigger and SCSN in z-direction, blue for the PASA signal given from one board to the other. The readout boards create the connection of the MCMs to each other to enable them to send the data and the calculated tracklets to the ORIs. The controlling of the MCMs, but also the controlling of the ORI (see Chapter 3.1.5), is done through the SCSN [GAR04], it is shown in Figure 3.6. The SCSN is divided into four linkpairs, counted from 0 to 3 for a C1 chamber and from 0 to 2 for a C0 chamber.

3.1.5 Optical Readout Interface

The Optical Readout Interface (ORI), shown in Figure 3.7, is a PCB board used to convert the electrical data into an optical signal. Two of them are sitting directly on the readout boards at positions 4 and 5, see Figure 3.6, close to the half chamber merger. The ORI provides an optical link with a rate of 2.5 GB per second. The optical output power of the ORIs varies typically between 300 μW and 600 μW. To sent it through the optical link it has to convert the incomming 240 Mbytes per second at a parallel input signal into the desired optical output. The optical link is done using a VCSEL (Vertical Cavity Surface Emmitting Laser) diode, which sends at a wavelength of 850 nm. The conversion process is done in a freely configurable complex programmable logic device (ispMACH 4k). The ORI board has a I^2C chip, which is reachable from the SCSN. It can be used for the control and the programming of the laser driver chip [LIN06].

To provide fast signals the chosen way to send the big amounts of data which is gained while data taking is the optical way.

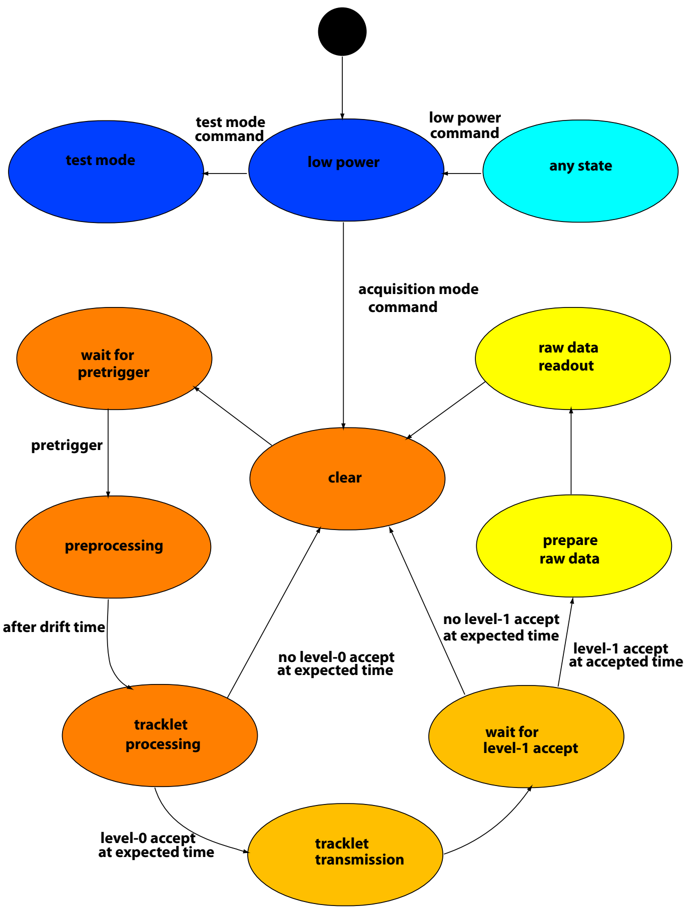

Figure 3.4: The global state chain of the TRD electronics (derived from [ANT06]).

3.1.6 DCS

The whole structure of the electronics on each readout chamber is controlled by a **D**etector **C**ontrol **S**ystem (DCS) board, see Fig. 3.8, it is sitting on the readout board at position 3, see Figure 3.6.

The detector control system controls and checks the detector (the chambers electronics) during operation. Additionally, it is responsible for powering up and down the detector, therefore it controls the voltage regulators on the readout boards. Without a running DCS board the detector is not operable. It is used to configure the frontend electronics, and it has to provide the clock and the trigger signals. In case of an emergency an appropriate response to the specific error will be initiated. To do so, several parameters have to be checked, namely temperature and power bus bar voltages. The measurement is implemented on the DCS board with a 12 Bit ADC, which can be used for all other measuring purposes too. The DCS board is a multi-functional and adaptive board. It is also used by the TPC, but with one major difference, the DCS board of the TRD is used at a 120 MHz clock instead the 40 MHz of the TPC version. The heart of the DCS board is an Altera FPGA, which enables the DCS board to perform its very different tasks. An ARM core is running the Linux operating system which enables the user interface, i.e. the possibility to access the DCS board via secure shell link. The DCS board has a 64 MB Flash EPROM and a 256 MB SDRAM. While booting, the necessary parts of the flash are mounted onto the SDRAM. For working purposes one should avoid writing and erasing data from the flash, every normal writing or erasing operation on the DCS board should be done on SDRAM, the reason for this is the limited writing cycles of the flash memory. The flash should therefore only be used for all long time keeping,

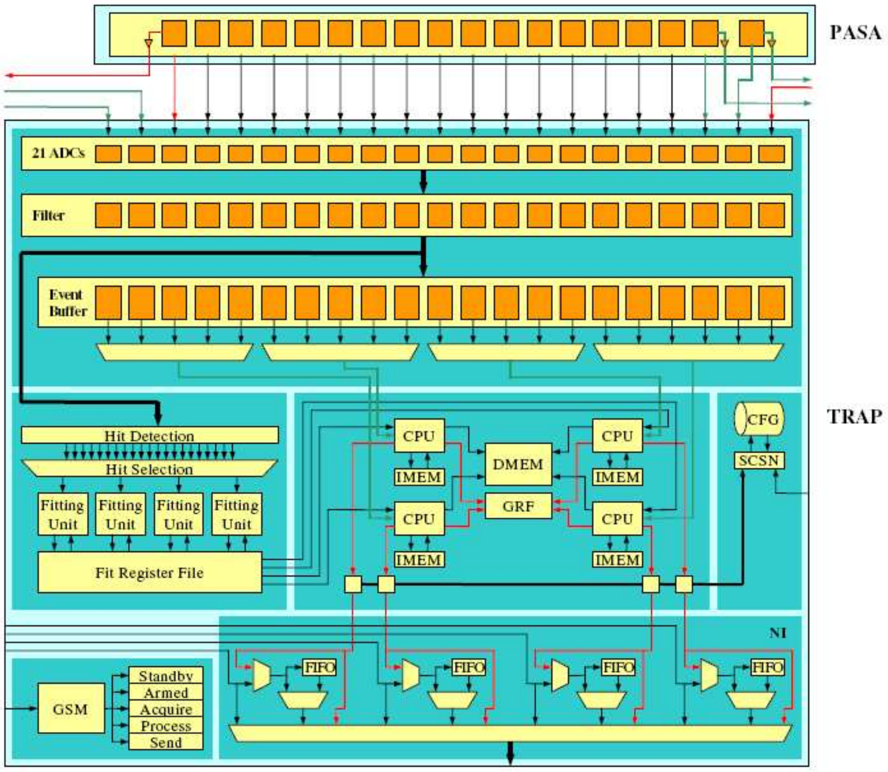

Figure 3.5: Overview of the structure of the TRAP chip (taken from [GUT06]).

e.g. linux kernel and other parts of the firmware [BAB06]. Each DCS board receives power from the DCS power distribution box (DCSPDB) [STE07], which sits inside each supermodule. The connection to outside the detector is done by ethernet connections (cat5e). During normal operation all commands go via ethernet through the DCS board via SCSN to the MCMs. For safety reasons a second command chain is implemented, the DCS board itself can also be controlled via its JTAG connection. All DCS boards are connected via JTAG in closed loops accross two layers. If the ethernet of one DCS board is not operable the command is send via ethernet to the given JTAG master which sends the command via JTAG to the DCS board without ethernet connection. The JTAG commanding level can also be used to program the FPGA of the DCS boards. The DCS boards also have a TTCvi optical connector and a corresponding TTCvi chip for processing the incomming optical signal. The signal, which is normally a trigger signal, is processed into an electrical signal which is sent to the MCMs via the SCSN on the ROBs.

Controlling Of The TRAP Chip

The controlling of the TRAP chip is done by instructions sent via the SCSN links. The commands are given via DCS board through the link. All controlling comands have to use this way. The second way to provide commands is the JTAG cable connection, which will be used in emergency cases to wake up a DCS board. But the command will still have to go to the link via DCS board. The commands are send as a 8 bit word. The main source for information about the controlling of the TRAP is the TRAP-Manual [ANT06].
Since the TRAP is configured, it is set to a wait pretrigger state. Depending on the global trigger status, the MCM will go into the next state when a trigger is received. In case of the noise measurements the

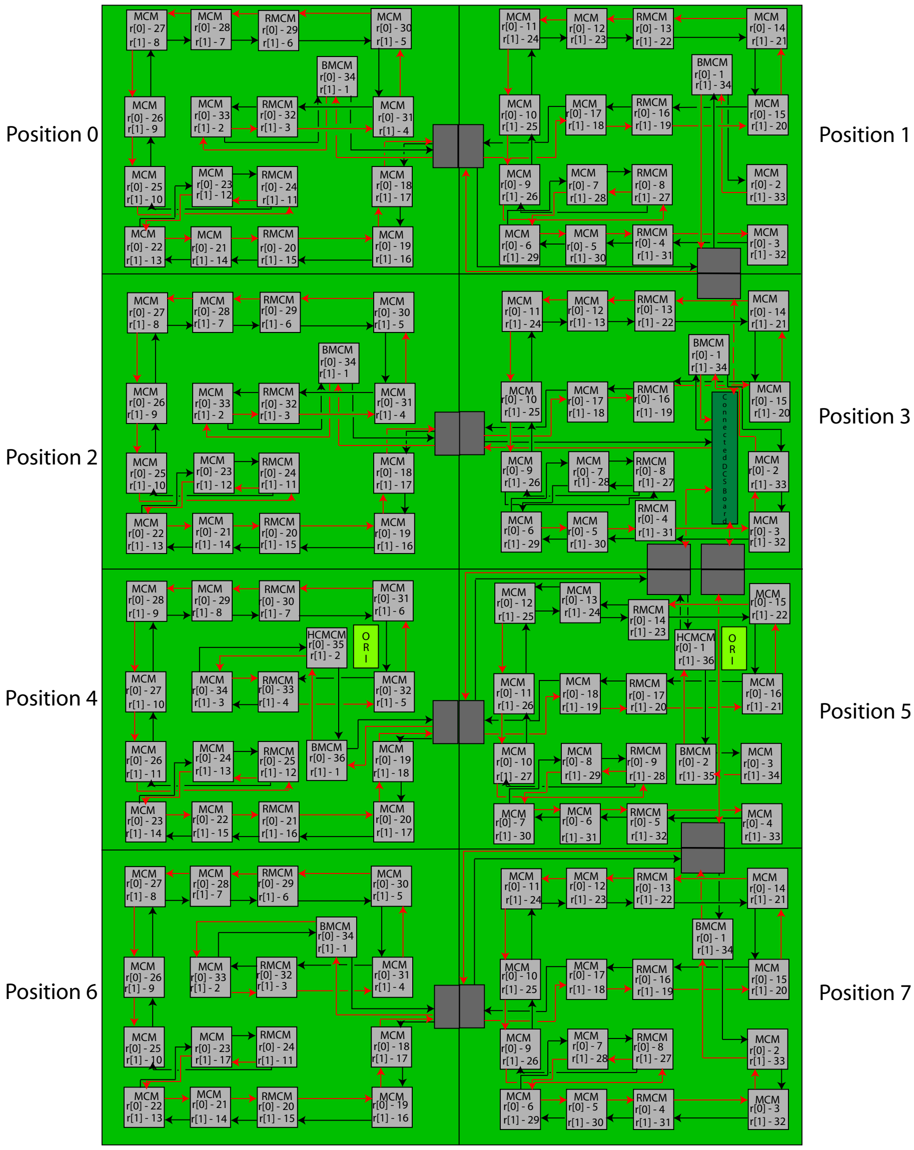

Figure 3.6: SCSN links of a C1 chamber.

whole readout has to be performed, therefore the MCM has to go through the trigger chain until level 2 accept is reached, the data is sent and after a clear state, the MCM goes back to the wait pretrigger state.

3.2 Readout

When the electronics is configured it is ready to perform the signal processing and the readout. There are two ways to readout the data of an event. It can be sent optically through the ORI or it can be read out via the DCS board.

Optical Readout And GTU

The optical readout is initiated by an incoming trigger when the MCMs are configured into a wait pre-trigger state. For the case of the single chamber data taking, a request for the optical readout is started

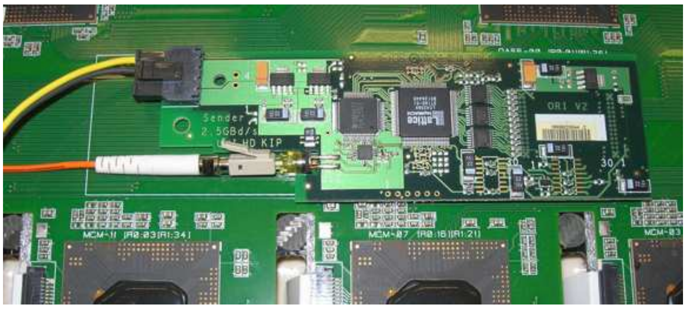

Figure 3.7: Picture of a ORI board mounted on a readout board.

Figure 3.8: Picture of a DCS board mounted on a readout board. With connected DCS power cable (red), ethernet (blue) and the optical TTC fibre (yellow).

with a script (opt_readout.sh). This is mainly done to initialize the ACEX cards. The ORIs are sending data every time the electronics is configured and a trigger is received. The readout flow is the following:

1. Three MCMs in a row are sending the data (ADC counts per time bin of each channel and tracklets) to the column merger (CM),
2. the four CMs of each readout board send to their board merger (BM),
3. the 3 or 4 BM provide the data to the half chamber merger (HCM),
4. each HCM forwards it to the ORI,
5. the ORIs are sending the data optically to the GTU.

The Global Tracking Unit (GTU) is the final operation mode to readout a supermodule. It also analyses the received tracklets and merges them to tracks. 5 independent Track Matching Units (TMUs) receive the data from one supermodule, which means that one TMU corresponds to one stack receiving data on 12 optical links. The TMUs with a large FPGA seek for global high-p_t tracks ($p_t > 3\,\mathrm{GeV/c}$) to create a trigger decission [LIP06].

DCS Readout

The DCS readout is used in case the supermodule can not be read out via the optical link. It has been used to readout data of the supermodule while testing in Heidelberg and at CERN. The DCS readout is

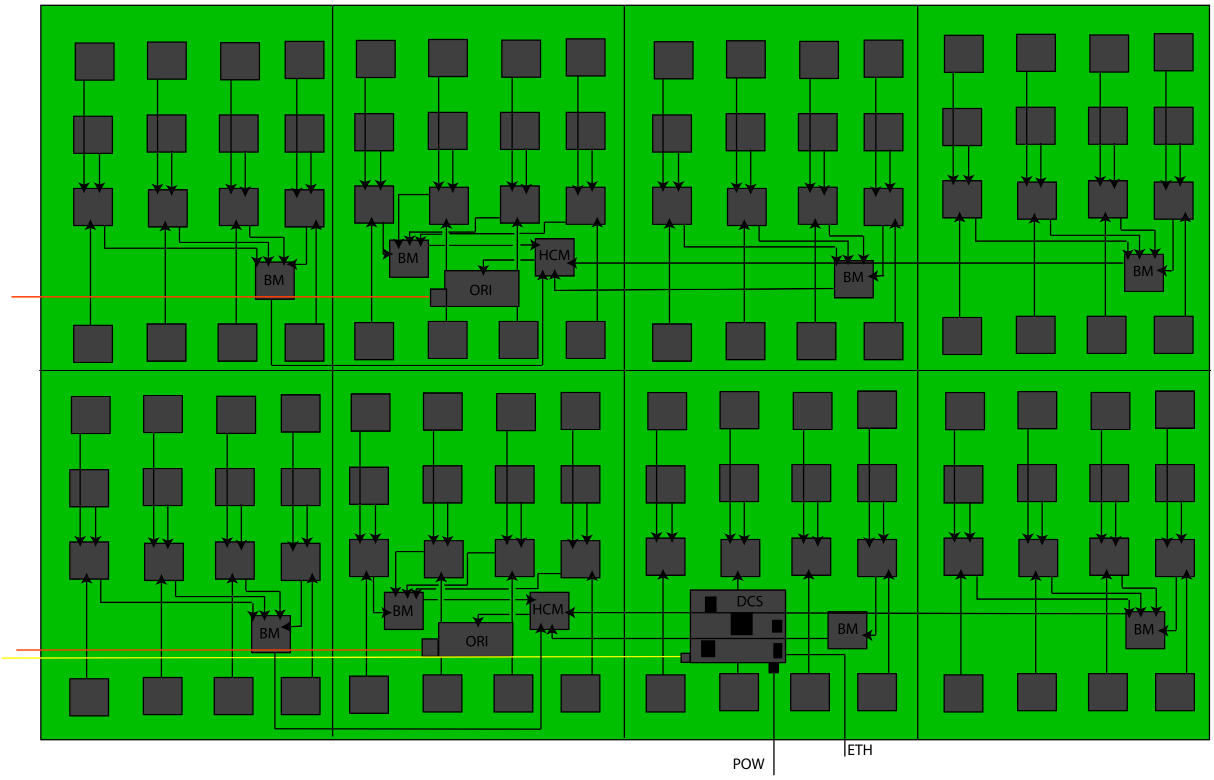

Figure 3.9: Scheme of the readout flow for a C1 chamber.

started through a script (dcs_readout.sh) which uses the following readout scheme:

1. Since the MCMs are configured and await a trigger signal to send the data like described in Section 3.2, a trigger will start the same sequence.
2. The HCMs which received all the MCMs information are requested to give the collected data to the DCS board, where the data is stored in two files (one per half chamber) locally on the SDRAM.
3. The data is then send via ethernet to the enquiring PC.
4. The data is processed into a ROOT file.
5. The two files stored on the DCS board are erased.

At CERN some data could be taken with a tentative setup, allowing to test the functionallity of the GTU.

Chapter 4

Electronics Integration And Chamber Testing

4.1 Electronics Integration

The Readout chambers are produced at five different sites, NIPNE (Bucharest), JINR (Dubna), GSI (Darmstadt), the University of Frankfurt and the University of Heidelberg.

Bucharest	Dubna	Frankfurt	GSI	Heidelberg
L1C0	L1C0	L0C1	L4C1	L0C0
L2C0	L2C0	L1C1	L5C1	L0C1
L2C1	L3C0			L1C0
L3C1	L4C0			L1C1
	L5C0			L2C0

Table 4.1: Distribution of chamber types for various constuction sites of the first supermodule.

For mounting the readout boards special screws have to be mounted. Therefore the screws have to be screwed to templates. The backplane has to be cleaned and then the screws can be glued into the foreseen holes. There are 96 screws to be mounted on each chamber with 8 readout boards (C1 chamber), and 72 screws on each chamber with 6 readout boards (C0 chamber). The templates should be fixed with weights and removed after one day when the glue had enough time to harden.
Before putting the readout boards a layer of a spacer made of polyethylene foam is stuck onto the back-panel, under the rows of MCMs, shown in Figure 4.1. They are fixed with double sided glueing tape close to the outcoming pad signal cable.
Before putting the readout boards on the chamber one should bent the signal cables a little in the direction of the connector they will go to. The readout boards, which have to be handled with care, are now placed on the chamber with a special fork tool. The tool is used to avoid the bending of the sensitive readout boards while moving. After mounting the readout boards, the DCS board and the ORI boards have to be installed. Prior to mounting the DCS board, a foil of kapton has to be placed on the readout board. The DCS board and the ORI boards should also be handled with care because of the pins they have to be connected to.
The next step is the connection of the boards to each other. This is done with the cable boards. They have different lengths and colours. The different lengths are necessary for the different chamber sizes.
Each readout board is fixed with 12 plastic washers and 12 plastic nuts onto the glued screws. The grounding of the readout boards is done with copper tape. The grounding connections are made from the

Figure 4.1: Picture of a chamber completely equipped with ROB spacers.

corners of the readout boards to the next readout board's corner. There is also a connection made to the chamber's aluminium frame. To reduce the resistivity of the grounding connection, the tape is soldered onto the readout boards. The part on the aluminium frame is screwed.

The cathode wire plane has to be connected to the nearest readout board ground, see Fig. 4.2.

As a last step of the ROB mounting the bent signal cables have to be inserted into the connectors on the ROBs.

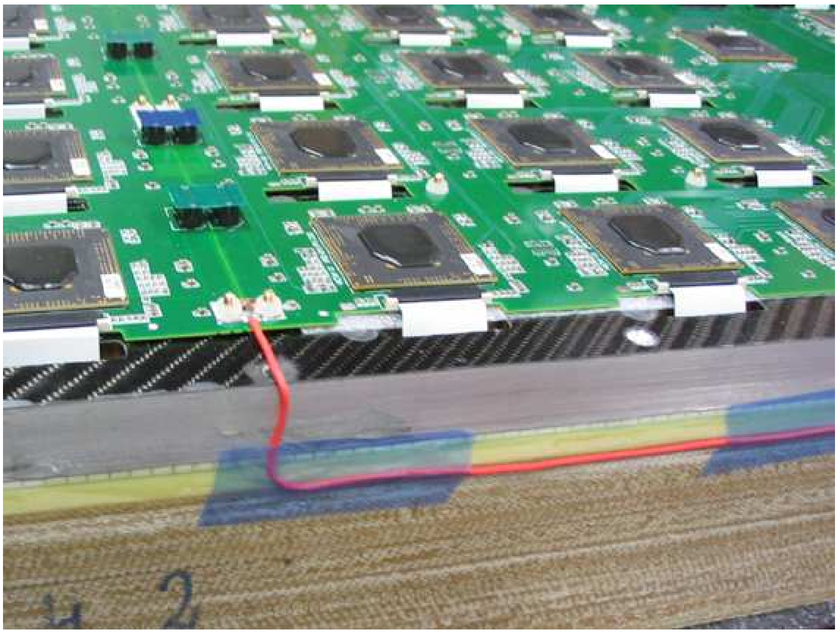

Figure 4.2: Picture of the cathode wire plane connection to the ground of ROBs.(The cable is visible in the foreground, running along the drift chambers side panel.)

The anode HV wires and the drift HV wire have to be connected to the HV filter board, the completed connection can be seen in Fig. 4.3. Therefore each cable, after proper preparation, has to be soldered onto the HV filter board. The fieldcage ground wire has to be soldered also onto the HV filter board ground, the filter board ground has to be connected to the nearest readout board ground, both can be seen in Figure 4.4.

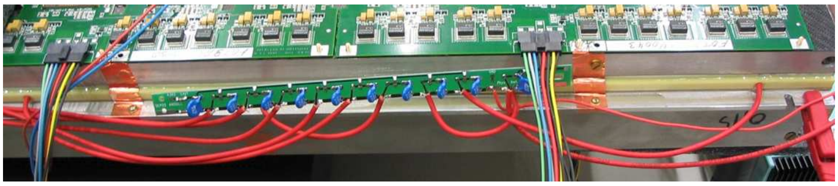

Figure 4.3: The filter box with soldered HV cables on the side of the chamber.

Finally the long high voltage cables have to be soldered onto the HV filter board to allow the connection of the chamber to the HV distribution box at the outer part of the supermodule. A picture of a completed chamber is shown in Figure 4.5.

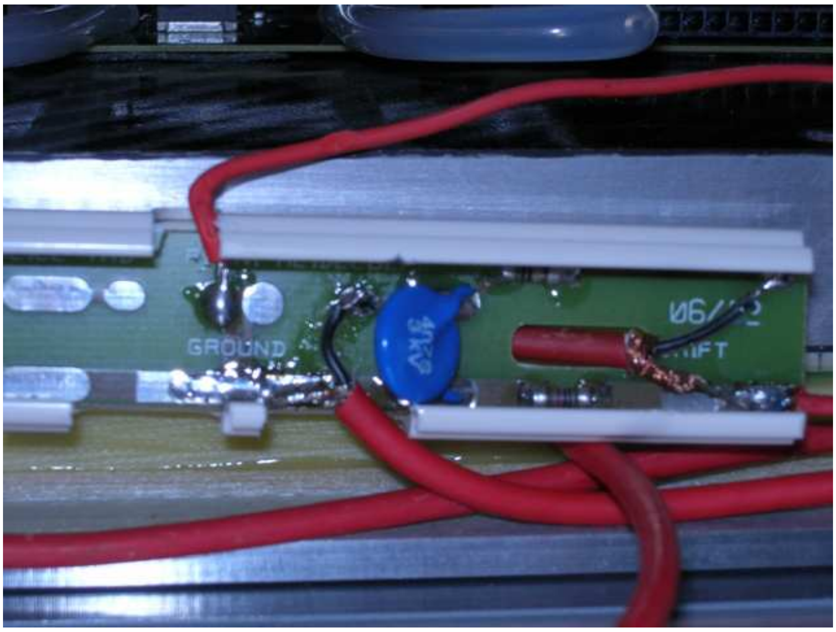

Figure 4.4: A detail of the HV filter board connections.

4.2 Test Setup

The test setup for the chambers of the first supermodule was built in the Kirchhoff Institute for Physics (KIP) in Heidelberg. The drift chambers are put on a table with all the needed connections associated. The power is provided for the DCS board by a single power supply which is also used to provide the chamber ground. The power for the readout boards is provided by another power supply with good stability to reduce noise. The same power source is used for the ORIs. The ethernet connection is set up as a subnet of the KIP network where all the needed computers were connected. A sketch of the setup is shown in figure 4.6. The trigger was done via a TTCvi setup controlled by DAQ07. The readout was done with two ACEX cards inside DAQ00, which saves the data directly to the harddisk of TRDRO1. The ACEX cards, which are multi purpose PCI cards developed at KIP, had to be used because the final GTU was still in development. TRDRO1 is used as the main testing PC. The configuration and controlling enviroment is build on TRDDCS02. For the control engine which provides the signals to the DCS boards, the intercomlayer is running to communicate with the feeserver on each DCS board.

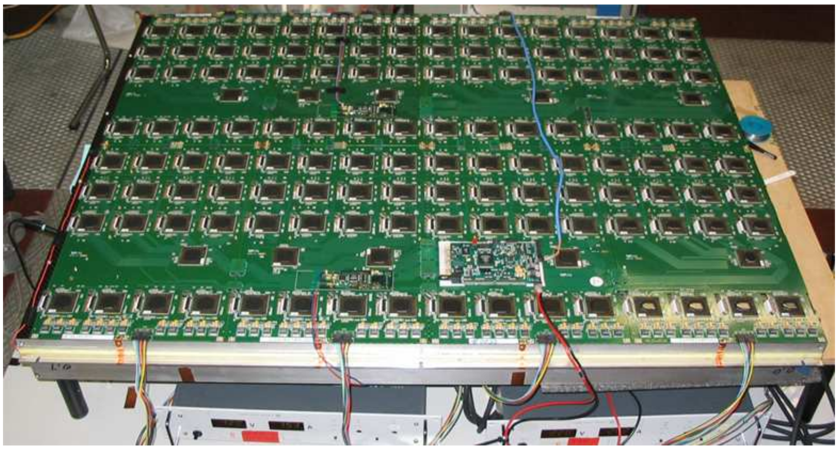

Figure 4.5: Completely equipped chamber with electronics on Stand 1

4.3 Testing Procedures

The testing of the front end electronics of each chamber is done with either bash shell scripts or perl scripts, the output is written into a logfile which covers many details of the test. The testing includes tests of the shutdown behaviour, the reset behaviour and the functionality of the multi chip modules and the readout board, which will be described in the following.

4.3.1 Preliminaries

Before starting with the tests of the front end electronics a directory for the new chamber has to be created. This is done with a script for relating the tests to one chamber in its given status. Since the person who did the equipping is not necessarily the same who does the tests the status of the chamber has to be checked. The status before the electronics testing should be that the chamber is equipped completely:

- The readout boards are mounted onto the chamber,
- the HV filter board is complete with the necessary capacitors,
- the HV filter board is in place and the high voltage cables of the cage have to be soldered onto the HV filter board,
- the HV grounds are soldered,
- the anode backwire is soldered to the correct position on the HV filter board,
- the drift cable is connected to the HV filter board,
- the cathode wire is grounded to the readout board ground,
- the HV filter board is grounded onto the closest readout board ground.

If everything is fine the script creates a new directory using the chamber number, date and information about whether the readout chambers electronics is equipped with cooling pipes, if so the name contains the remark wcp (with cooling pipes).

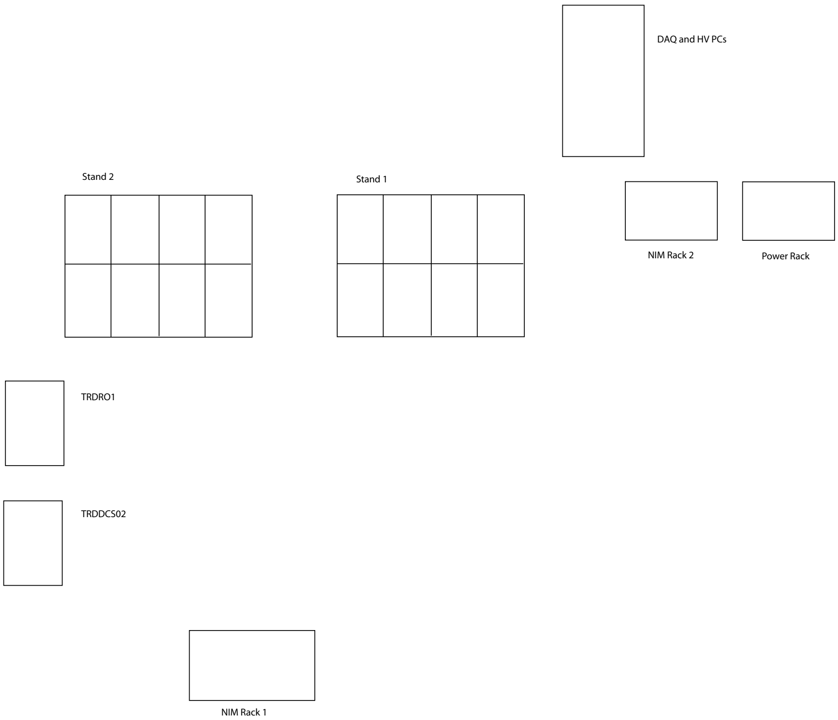

Figure 4.6: Schematic drawing of the ROC testing setup

4.3.2 Shutdown Test

The shutdown test controls the shutdown behaviour of the voltage regulators. It is tested with powering up certain ROBs and sending pings to all MCMs to see if they are alive.

1. All ROBs are switched off. This means pinging all linkpairs (SCSN connections) should show that no MCM is answering.

2. Linkpair 2 is powered, since the halfchamber mergers are here which distribute the clock to all MCMs it is necessary to start here. Pinging all linkpairs should show an answer only of the 36 MCMs (16 MCMs, 1 BM and 1 HCM $\times$ 2) on linkpair 2.

3. Linkpair 0, which is the first linkpair, is powered also. This means that 34 MCMs on linkpair 0 and 36 MCMs on linkpair 2 should answer the ping.

4. The power for linkpair 0 is switched off again, but linkpair 1 receives power. This means that 34 MCMs on linkpair 1 and 36 MCMs on linkpair 2 should answer the ping. This would be the complete test for a C0 chamber. For a C1 chamber there is also,

5. Instead of linkpair 1, linkpair 3 receives power now. So that 36 MCMs on linkpair 2 and 34 MCMs on linkpair 3 reply to the pinging of the whole chamber.

The test is completed with a positive result when all powered linkpairs answer to the ping.

4.3.3 Reset Test

The reset test is done to check the functionality of the reset capabilities of the MCMs. The reset test is started by a ping with given low voltage to the whole electronics to check if all MCMs can be reached via

SCSN lines. For ensureing this, a complete ping of the chamber is perfomed and the status is checked. If all MCMs are answering, this part of the test is performed correctly. Now the script is forcing the writing of some defined data into each MCM. This information is read via slow control network and it is checked if it is correct. If everything is correct either 104 (16 MCMs, 1 BMs $\times$ $6+2$ HCMs) or 138 MCMs (16 MCMs, 1 BMs $\times$ $8+2$ HCMs) have the right values in their register. In the next step all MCMs are reset. After that each MCM is checked if it is in a reset state. If this is the case the test is performed correctly and all either 104 or 138 MCMs are in the reset state.

4.3.4 Control Engine Tests

The next tests are performed through the control engine (CE). For these tests the intercomlayer is used to provide the communication with the electronics. The intercomlayer is fed by the given tag, corresponding to a certain test. There are seven tags to perform different kind of tests. More tags exist mainly for chamber configuration via the CE, which will finally lead to the configuration with PVSS.

1. The test to check the network interface (NI) of the slow control serial network. The control engine sets the parity bit and false bit to a defined position. Then it is sending a series of 7 patterns through the network and checks the read value. After that the parity bit and false bit are set to another defined position. A series of 7 patterns is again sent to the network and read. If some patterns differ from the sent ones the program evaluates the broken bits, for the broken bit and the corresponding MCM.

2. The second test via control engine is the ORI test. It is testing the communication through the optical readout interface, i.e. the communication from half chamber merger to the ORI. Therefore it is sending a pattern to the ORI lines. The test is also performed as good if the ORI pins on the readout boards are bridged. This means the test is just checking the connectivity of the device.

3. The bridge test. It is testing the bridgeing ability of the MCMs. This has to be used to close a readout link in the case that a MCM is broken, to still have a closed communication chain. For this reason it is succesivesly setting every MCM to the bridge mode. While bridgeing it is sending a pattern on link 0 and that should return on link 1. This is done for all linkpairs and all MCMs.

4. The next performed test is the reading of the laser IDs of the given MCMs. The main reason is to test if all MCMs have a laser ID. On some MCMs the laser ID is not readable through the SCSN. This is recorded in the database (Gate DB).

5. The test of the DMM.

6. The test of the DDD.

7. The test of the IMM.

All three memory tests (DMM, DDD and IMM) are performed identically. For testing the memories, a defined value is written into the register. After that a pretrigger is given. This leads the memeory to move the value into its register to the NI memory. The NI memory is read via SCSN and the values are compared.
Since the CE tests identify errors in data lines and SCSN links, the evaluated data can be used to fix the lines.

4.3.5 Reading Laser IDs

For the purpose of identification of a MCM in the supermodule all MCMs should have a unique identification code in the database. Ideally all MCMs would have an unique laser ID. However, some MCMs don't have any readable laser ID or some MCMs have equal laser IDs. For these cases it was tried to find a good combination of variables. It is now done with combining the laser ID with the MCM ID. The MCM ID is a number written on the label of each MCM during their production. To test the uniqueness of the identification of each MCM the program looks up the laser ID in the database and checks its uniqueness. If it is unique it goes on with the next MCM untill the chamber is completely checked. If it is not unique or broken the test operator is asked to provide the MCM ID.

4.3.6 Noise Measurements

For measuring the noise of the electronics the MCMs are configured for data taking with different configurations:

1. Without any filter switched on (nf= no filter),
2. with pedestal subtraction (p),
3. with pedestal subtraction, gain correction and tail cancellation (pgt).

For inducing a signal inside the chamber a pulser was used. It is using the trigger coming through TTC to synchronize the sent pulse, a TTL signal, and the measurement. This pulse is introduced to the chamber via the cathode wire. This can be used to detect not connected channels, because they will not receive the pulser signal. Therefore the electronics was configured with only pedestal subtraction.
For data taking the trigger was sent directly to the DCS board via optical fibre. The data is sent to the DAQ PC optically through the ACEX cards. The data is stored locally and also in the working directory of the given test. To check the data ROOT is used to visualize and evaluate the chamber's noise (Fig. 4.7). It shows for every chamber four plots, the baseline distribution for each pad, a high granularity rms for each ADC channel corresponding to a pad, the accumualtion of the rms according to the MCMs and the average rms per readout board. This is necessary to see correlations of certain kinds. ROOT is also used to have a detailed view on the temporal development for each pad per timebin (Fig. 4.8). It shows in x the pads in φ direction, which are corresponding to the 21 ADC channels ($21 \times 4 \times 2 = 168$), and in y the 30 timebins for each pad ($30 \times 16 = 480$).
The ROOT visualization is accomplished via perl scripts. All measurements were performed with 100 triggers so 100 events can be accumulated for the noise/pulser measurement. Just for shots of the MCM status only a single trigger was sent. This is sometimes necessary when some MCMs do not get back into the right global state. In the beginning some readout boards have real problems with proceeding the configuration. It was necessary to switch off certain MCMs or just switch off some ADC channels of these MCMs (masking). In that case a software patch was created.

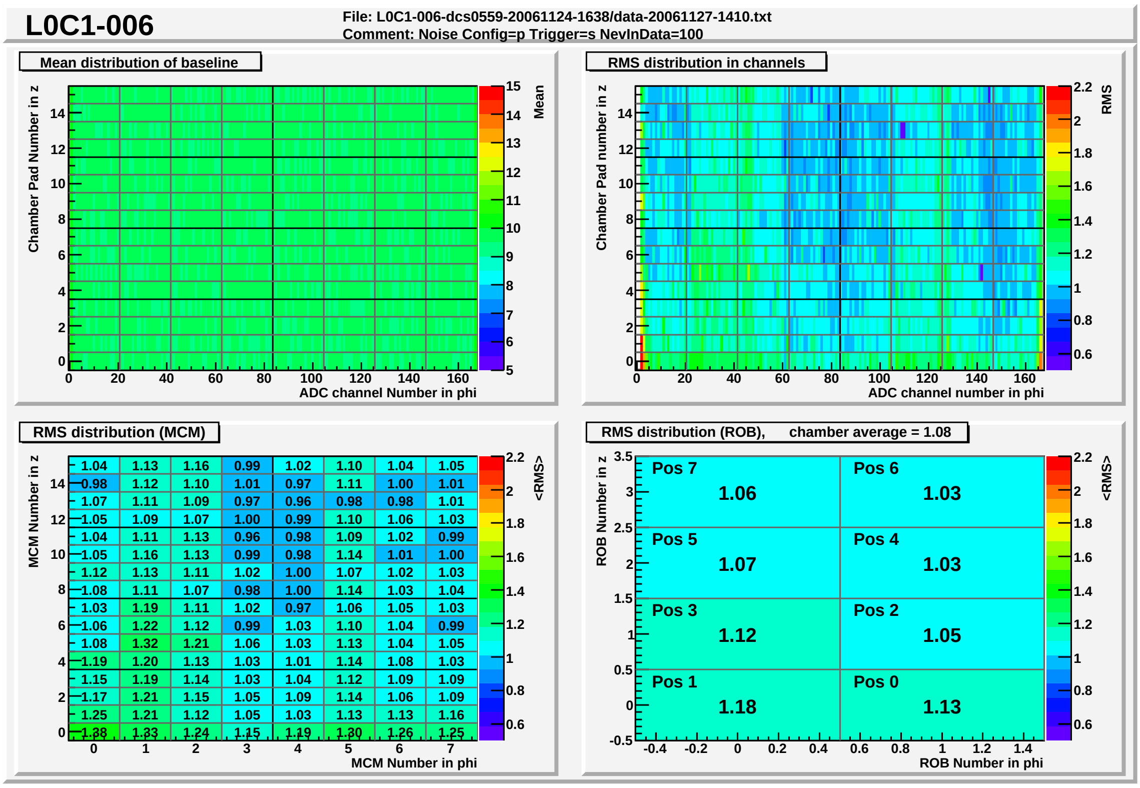

Figure 4.7: Example of a noise plot of a C1 chamber of layer 0 with pedestal configuration

4.3.7 Stress Test

The stress test is the sending of a large number of triggers over a long time to test the stability of the chamber. Therefore the front end electronics is configured. For normal testing the electronics is configured in the p configuration, with only pedestal substraction. In some cases also a pgt (pedestal substraction, tail cancellation and gain correction) stress test is done. At a later stage, while testing the supermodule some more types of stress tests are performed. The testing is done in terms of short tests (from ten minutes up to one or two hours) and with long time stress tests for at least eight hours. The long time stress test was performed at least once for the electronics of every chamber inside the first supermodule.

4.4 Test Results

The results of the tests were saved in the corresponding directory to each testing procedure. The noise values and the corresponding number of dead MCMs and ADCs are summarized in Table 4.2. Dead MCM means the MCM can not be used for data taking, reasons for this are too high noise and connected to this the bad processing properties for tracklets.
Dead channel means blind channels, i.e. channels which have no connection from the pad to the PASA or some have bad connections from the PASA to the digital part of the MCM.
The average noise (rms) of the ADC channels has reached the recommended values for all chambers. A noise of 1.00 corresponds to the recommended 1000 electrons which the eltctronics is designed for. The chamber L1C1-020 is an exception but just for the final tests, it was fine for the first tests, before the cooling pipes were mounted, and it is fine in the supermodule. The high average noise of this chamber seen in the Table 4.2 is due to the test setup (Stand 2), which was only used for the final tests of this

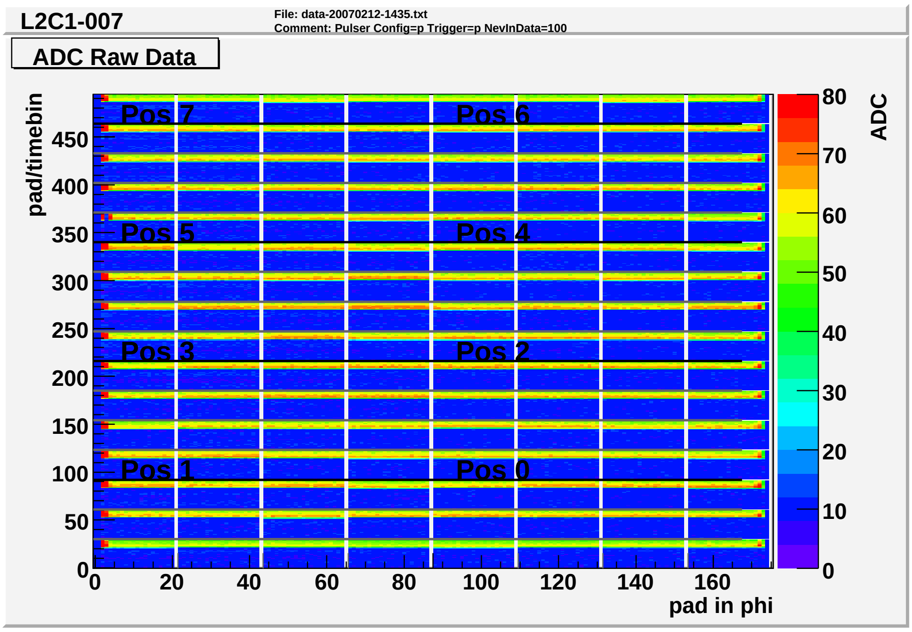

Figure 4.8: Example of a pulser plot of a C1 chamber of layer 2 with pedestal configuration. The timebins are shown for the first of the 100 events taken.

chamber. Stand 2 has been mainly used to debug electronics problems.
The increasing of the noise from layer to layer can be explained by the increasing pad size.
The measured noise corresponds directly to the capacity which is mainly given by the pad geometry.
To clarify the statistics of the noise data a histogram for the three different configurations has been created. An example is shown in Figure 4.9. It shows the counts of different noise (rms) values of the ADC channels, for data with nf (red), p (blue) and pgt (lavender) configuration.
The higher noise for the pgt configuration is due to the high processor activity in the TRAP. The two further activated filters are increasing the digital power consumption which leads to higher noise due to parasitic couplings. The tail cancellation filter of the TRAP chip is a differentiator which increases the noise for the tail part of the signal, since noise has no tail part the structure with pgt configuration in the histogram can be explained as the processing of the tail cancellation filter in the TRAP chip with no real tail.
In appendix A the noise histograms for all configurations of all chambers from their final test are given.

Chamber	Final test date	Average noise (rms)			Dead MCMs	Dead ADCs
		nf conf.	p conf.	pgt conf.		
L0C0-015	18/07/2006	1.14	1.15	1.33	0	0
L0C1-001	19/07/2006	1.09	1.11	1.26	0	3
L0C1-002	29/07/2006	1.16	1.19	1.30	4	0
L0C1-003	20/07/2006	1.10	1.10	1.29	0	2
L0C1-004	20/07/2006	1.10	1.10	1.28	0	0
L1C0-008	26/07/2006	1.26	1.27	1.43	0	5
L1C1-002	02/08/2006	1.09	1.18	1.18	0	4
L1C1-011	07/08/2006	1.49	1.17	1.33	0	0
L1C1-019	21/07/2006	1.22	1.26	1.36	0	0
L1C1-020	05/08/2006	3.04	3.08	3.15	0	4
L2C0-005	10/08/2006	1.19	1.22	1.22	1	5
L2C1-001	09/08/2006	1.12	1.13	1.34	0	1
L2C1-003	11/08/2006	1.15	1.16	1.31	0	2
L2C1-005	10/08/2006	1.11	1.15	1.51	1	0
L2C1-018	11/08/2006	1.13	1.15	1.34	0	2
L3C0-008	12/08/2006	1.24	1.17	1.54	1	0
L3C1-017	16/08/2006	1.28	1.25	1.43	1	21
L3C1-021	15/08/2006	1.14	1.16	1.35	0	0
L3C1-023	15/08/2006	1.15	1.18	1.41	0	1
L3C1-031	19/08/2006	1.22	1.22	1.43	0	1
L4C0-018	21/08/2006	1.34	1.27	1.54	0	8
L4C1-003	28/08/2006	1.21	1.21	1.44	0	0
L4C1-004	23/08/2006	1.43	1.51	1.62	1	0
L4C1-008	19/08/2006	1.23	1.21	1.46	2	6
L4C1-011	22/08/2006	1.18	1.18	1.39	0	9
L5C0-001	26/08/2006	1.20	1.20	1.44	0	1
L5C1-003	30/08/2006	1.23	1.25	1.50	0	3
L5C1-004	30/08/2006	1.28	1.29	1.48	0	3
L5C1-034	27/08/2006	1.18	1.20	1.41	1	2
L5C1-035	28/08/2006	1.24	1.24	1.44	0	2
Sum:					12 (0.33%)	85 (0.11%)
Average:		1.20(6)	1.20(6)	1.39(6)		

Table 4.2: Final results of the tests of the readout chambers before going into the supermodule.

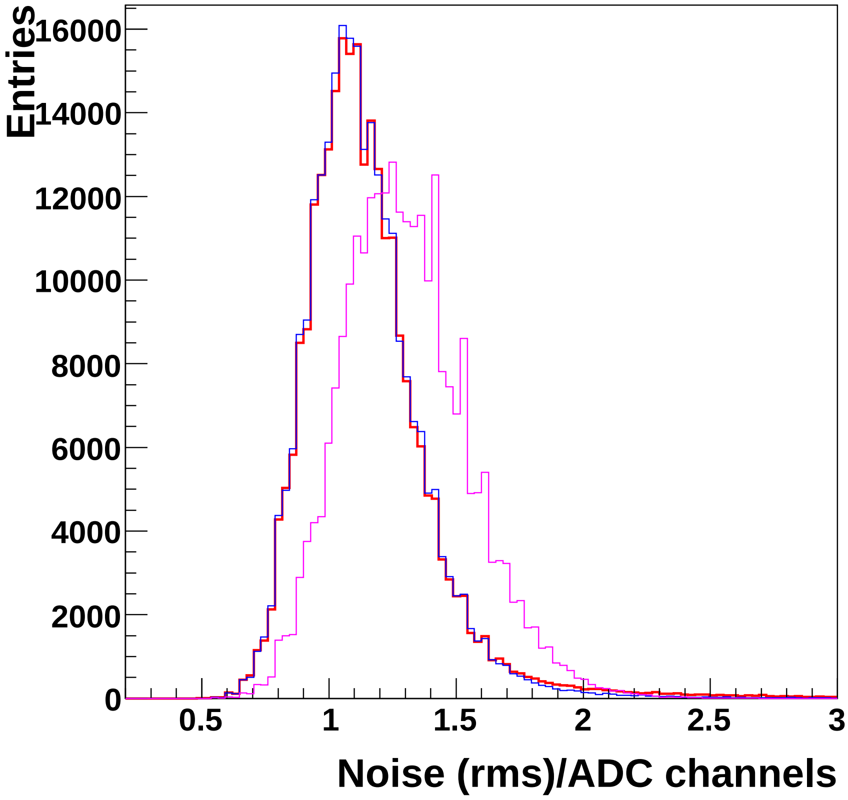

Figure 4.9: Example of a noise histogram (chamber L1C1-020 for the first tests, the average noise (rms) is 1.09).

Chapter 5

Supermodule Assembly And Testing

5.1 Supermodule Assembly

The assembly starts with the mounting of cables and the related connectors on the power bus bars. As the power bus bars are electrically insulated by kapton tape, to screw the brass screws which make the electrical contact from the connector on the readout board side to the power bus bar, the kapton has to be removed partially at the thread of screw. The cooling bars are attached onto the sidewalls with special cramps. The power bus bars are fixed with tape onto the cooling bars. The completed side walls are then connected to the two big inner frames of the supermodule to increase the stability. After the mounting of the frames on the bottom part, the main mechanical part of the supermodule is completed.
Now the installation of the chambers and cables begins. A shot of the assembly process can be seen in Figure 5.1 and the corresponding layout of a supermodule in Figure 5.2.
The procedure for each layer is very similar just the connection plates are mounted into the supermodule in a special order. The readout chambers are inserted into the supermodule, with special care. The chambers are lowered into the supermodule using two long belts/ribbons held by four people. The chambers within a layer are connected to allow the gas flow via special connectors on the lateral chamber frames. When all chambers of one layer are lowered in, the cabling begins.
The necessary cables for the layer are produced with a defined length. The long high voltage cables going from each chambers HV filter box to the HV patch panel are layed properly into the gap between the chambers side and the side wall of the supermodule. Then the power connectors on this side are then connected. For the counter side the cables are layed into the other sides gap. Two kinds of cables are going towards the side where the DCSPDB sits, these are DCS power cables and the ethernet cables. The JTAG cables are laying inside the gap connecting one DCS board to another. From the two outer chambers, on the side where the HV is connected, sensing wires are connected to the LV filter boxes mounted on the edge of the power bus bars to measure the actual voltage on the bus bar. After placing all these cables, into the gap between the chamber and the side wall, the power connectors are applied to the readout boards. The next cables are three optical fibres going to each chamber, there are two orange readout fibers (ORI fibres), connecting the ORI to the optical link patch panel, and one yellow TTC fiber, coming from the Schütten box. The Schütten box is a cable box in which all TTC fibres are connected to one TTC input. The readout fibers are numbered corresponding to the chamber and layer. The first figure gives the layer, so the numbers are given from 0 to 5. The second figure is from 0 to 9 with the odd numbers are connected on the HV side and the even ones on the counter side. One has to be careful because the fibers are very sensitive. The cables are routed in certain ways. The ORI fibers are routed below the ORI and the DCS cooling pipes and have to go very close to the ORIs themselves through the frames. To connect the fiber to the ORIs a clipping tool was produced and has to be put onto the ORI. Each TTC fiber is routed along the middle of the chambers through the supermodule and is just turning

to its DCS board, to be connected. The TTC fibers have their own connectors. For both types of optical fibers one should avoid any mechanical tension.
Now the flexible tubes of the cooling pipes are connected to the pipes welded onto the cooling bar.
After checking and testing the functionality of the cables and fibres, special connection plates are mounted to ensure the mechanical stability and the same scheme can begin for the next layer. The final layout of the supermodule can be found in Table 5.1.

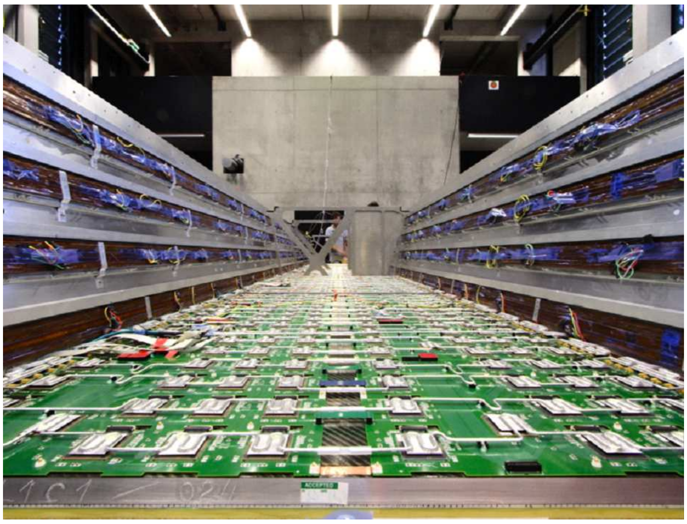

Figure 5.1: Picture of the supermodule in the experimental hall during assembly. (Two layers are already mounted. The power bus bars and the ROB power cables can be seen on the side walls on either side of the supermodule.)

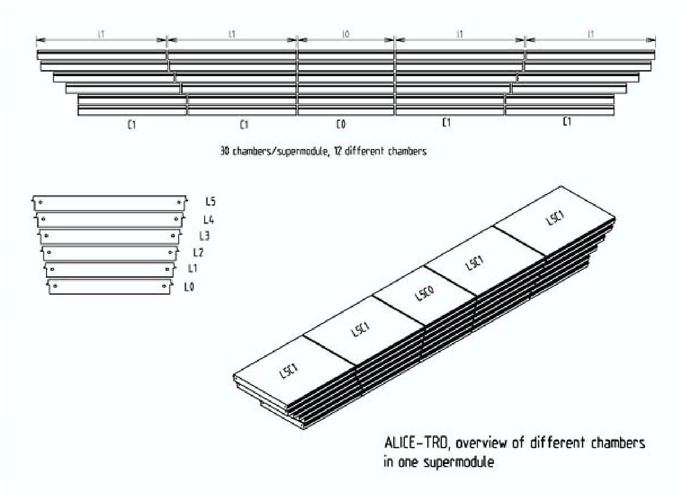

Figure 5.2: Layout of the readout chambers in the supermodule without the services and the frame.

	Stack 0	Stack 1	Stack 2	Stack 3	Stack 4
Layer 5	dcs0421 L5C1-003	dcs0429 L5C1-034	dcs0414 L5C0-001	dcs0425 L5C1-035	dcs0427 L5C1-004
Layer 4	dcs0415 L4C1-011	dcs0428 L4C1-008	dcs0533 L4C0-018	dcs0418 L4C1-004	dcs0490 L4C1-003
Layer 3	dcs0420 L3C1-031	dcs0406 L3C1-021	dcs0419 L3C0-008	dcs0535 L3C1-023	dcs0400 L3C1-017
Layer 2	dcs0409 L2C1-018	dcs0408 L2C1-001	dcs0410 L2C0-005	dcs0407 L2C1-003	dcs0411 L2C1-005
Layer 1	dcs0531 L1C1-011	dcs0426 L1C1-019	dcs0532 L1C0-008	dcs0422 L1C1-020	dcs0530 L1C1-002
Layer 0	dcs0529 L0C1-004	dcs0423 L0C1-002	dcs0525 L0C0-015	dcs0527 L0C1-001	dcs0526 L0C1-003

Table 5.1: The final supermodule layout, showing the location of each chamber and DCS board in the supermodule.

5.2 Tests Of The Supermodule

5.2.1 Testing Of The Supermodule During Assembly

During the assembly of the supermodule the functionality of the assembled system is tested. The used setup is sketched in Figure 5.4. Therefore the necessary parts are powered up. The power is given by the Wiener power supplies (see Figure 5.3), which will be used as the final power supplies in the experiment. This was done to study the behaviour of the supplies but also to develop the necessary software which will be needed in the experiment. The controlling is done by a PVSS module.
The testing begins after a whole layer of the supermodule is completed, including all cables and connections.
The test of the functionality mainly means checking whether a secure shell (ssh) communication is possible and whether the chambers can be powered up completely, i.e. that no shorts are existing. While the chamber is powered the optical output of the ORIs is measured, to ensure the power of the laser diode is still high enough to guarantee a sending of data through the several optical patch panels that will be between the ORIs and the GTU in the final installation. An example measurement is shown in table 5.2.
To ensure the detector functionality the chambers are configured and readout. For single chambers this can be done via ACEX card. In the case of a layer or a supermodule this is done with the GTU or via ethernet (DCS readout). So the noise data is mainly taken with DCS readout. Using the noise data of each layer several noise sources have been located and eliminated. One example is the high induced noise from JTAG cables, which has been resolved by shielding the cables with copper foil.

JTAG Chain

The JTAG chain is tested when a JTAG chain loop is completely connected. The test itself is done in the following steps:

- Beginning a secure shell connection to the master DCS board.
- Doing a secure shell to the slave DCS board through the JTAG connection.
- Giving the command to reboot via JTAG.
- Waiting until the slave, i.e. the rebooted, DCS board is accessible through JTAG.

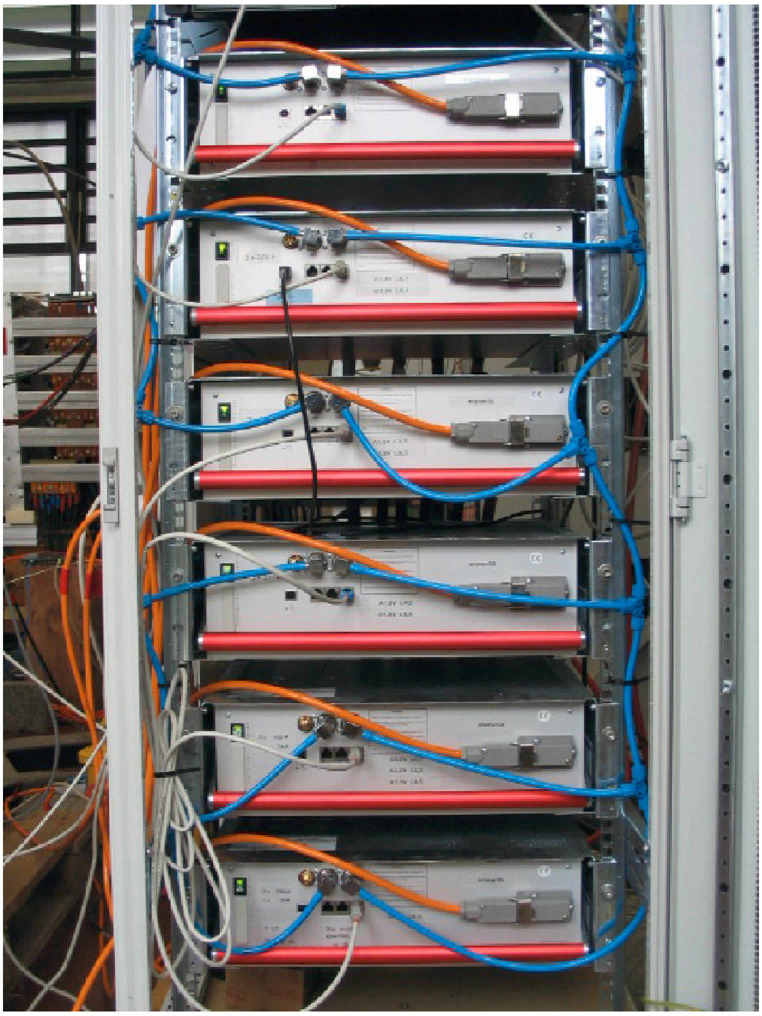

Figure 5.3: Picture of the WIENER power supplies used for powering the supermodule and to develop the control software.

This is done for every DCS board of the two layers, the JTAG chain consists of.

Gas Tests And Cooling Tests

When two layers are completed, to test the gas tightness, these two layers are connected to create a gas circuit. The chambers are filled with nitrogen and the leak rate is measured. The results for the performed measurements are shown in Table 5.3.

When three layers are completed, the cooling is tested. Temperature measurements are performed at the DCS boards (the temperature sensor measures the surrounding temperature, so it is more an enviromental temperature close to the DCS board). Temperatures can also be measured on the MCMs and in this case the relative stability is monitored. Even so, T can be calibrated in principle.
To check the temperatures measured with the DCS boards a monitoring program has been developed. Since the tests have to be done overnight a software interlock was developed which has to shut down the low voltage in the WIENER power supplies if the temperature, measured on the DCS board, is above a certain value which can be set (generally this value is set to 305 K).

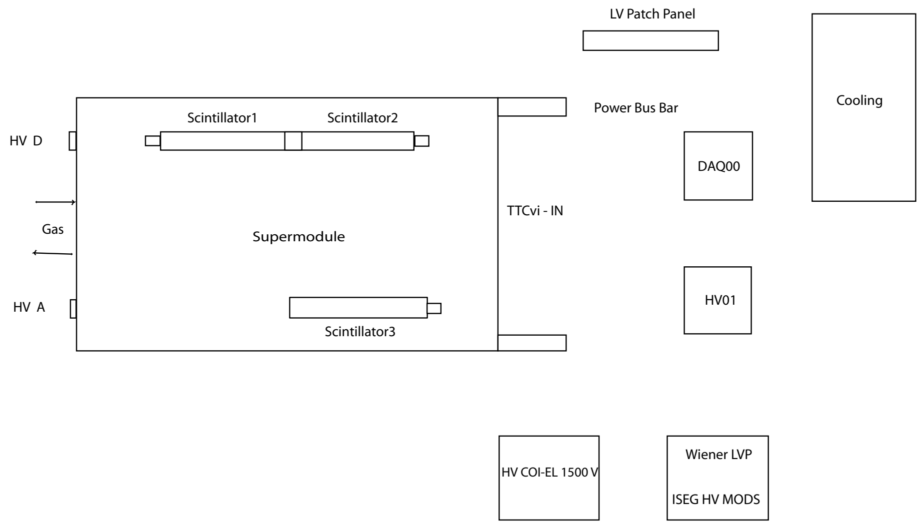

Figure 5.4: Scheme of the setup used in Heidelberg to test the supermodule.

		Stack 0	Stack 1	Stack 2	Stack 3	Stack 4
Layer 4	B-Side	399.1	350.0	342.1	326.7	401.8
	A-Side	403.8	387.4	269.7	198.6	458.3
Layer 3	B-Side	297.9	264.8	329.6	422.8	383.8
	A-Side	318.4	389.0	346.7	434.7	447.9
Layer 2	B-Side	347.7	352.4	371.5	353.1	437.6
	A-Side	353.1	401.0	371.5	353.1	437.6
Layer 1	B-Side	330.4	385.6	342.8	421.7	385.6
	A-Side	360.0	325.8	384.6	439.7	280.5
Layer 0	B-Side	411.2	359.9	369.0	371.0	366.5
	A-Side	377.6	385.6	385.6	459.2	295.1

Table 5.2: Typical optical output power measurement done in Heidelberg (values in microwatts).

5.2.2 First Tests With The Completed Supermodule

The first tests of the complete supermodule are tests of the configuration and the readout of all chambers. Therefore some new scripts have to be developed to configure the supermodule, to be able to take data and to plot the received data but also to be able to stress the supermodule with different trigger rates. A sample plot of the whole supermodule noise can be seen in Figure 5.5, the chamber at layer 0 stack 2 is no longer configurable since the supermodule has been completed, it does not receive any low voltage for the digital channels. For emulating the situation of the supermodule trigger chain, several new configurations have to be accounted according to loops over the global states of the MCMs for Level 0 accept, Level 1 accept and only pretriggers given, since the sending of data corresponds to Level 2 accept. The rates for the different trigger chain loops can be seen in Table 5.4.

High Voltage And Cosmic Rays

For tests of the high voltage and to take cosmic ray events the supermodule is flushed with a mixture of Ar/CO_2, the used mixture is 85% argon and 15% CO_2. To test the high voltage first the high voltage has to be connected, this is done for the anode and the drift HV seperately. The connection of the high voltage cable already, leads to an increase of the noise of the outer pads of the chambers inside the supermodule.

Layers	Leak rate l (mbar ml/h)	Average l per chamber (mbar ml/h)
4 & 5	4.0	0.4
2 & 3	6.8	0.68
0 & 1	2.7	0.27

Table 5.3: Leak rates of the gas distribution measured with nitrogen for the first supermodule during assemly in Heidelberg.

Trigger state	Rate (kHz)
Level 2 accept	1
Level 1 accept	3.4
Level 0 accept	200
Pretrigger	500

Table 5.4: Rates of triggers which the electronics is designed for, which also corresponds to possible rates in p-p collissions.

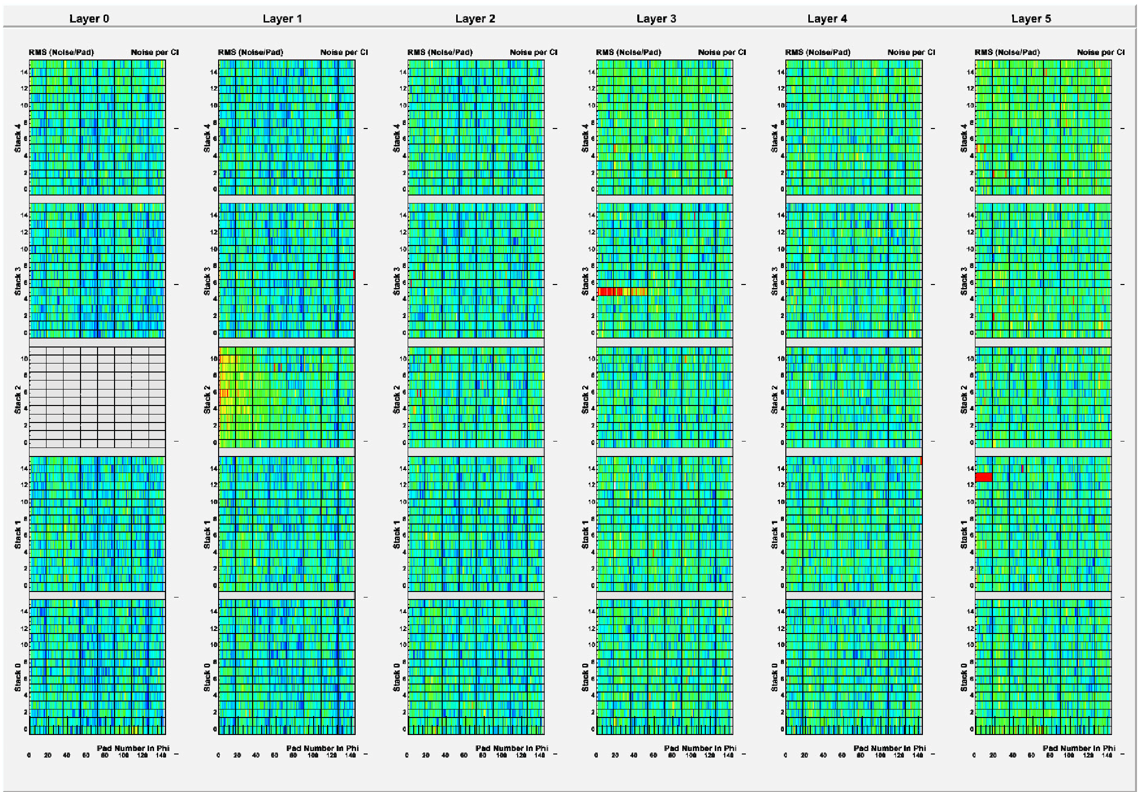

Figure 5.5: Example noise plot for all the chambers in the supermodule taken in Heidelberg.

The ramp-up of the channels of the high voltage can be done with the ISEG control panel. To test the complete performance of the supermodule cosmic rays are used. Therefore a coincidence trigger, made by three scintillators is build. The high voltage for the scintillators (≈ 2000 V) is given by a single HV power supply, the coincidence is done with a NIM coincidence module. The setup of the scintillators can be seen in Fig. 5.4, they are laying on the ground, just supported by some foam to prevent damage of the scintillators; two are laying partially on each other one is laying seperately. A script is developed to readout the data produced by the cosmic rays for the whole supermodule with DCS readout.

Several single cosmic ray events were taken at Heidelberg before the supermodule was shipped to CERN. The first shower can be seen in Fig. 5.6. Another event is shown in Fig. 5.7, an ALIROOT display of a cosmic ray event taken in Heidelberg is shown in Fig. 5.8.

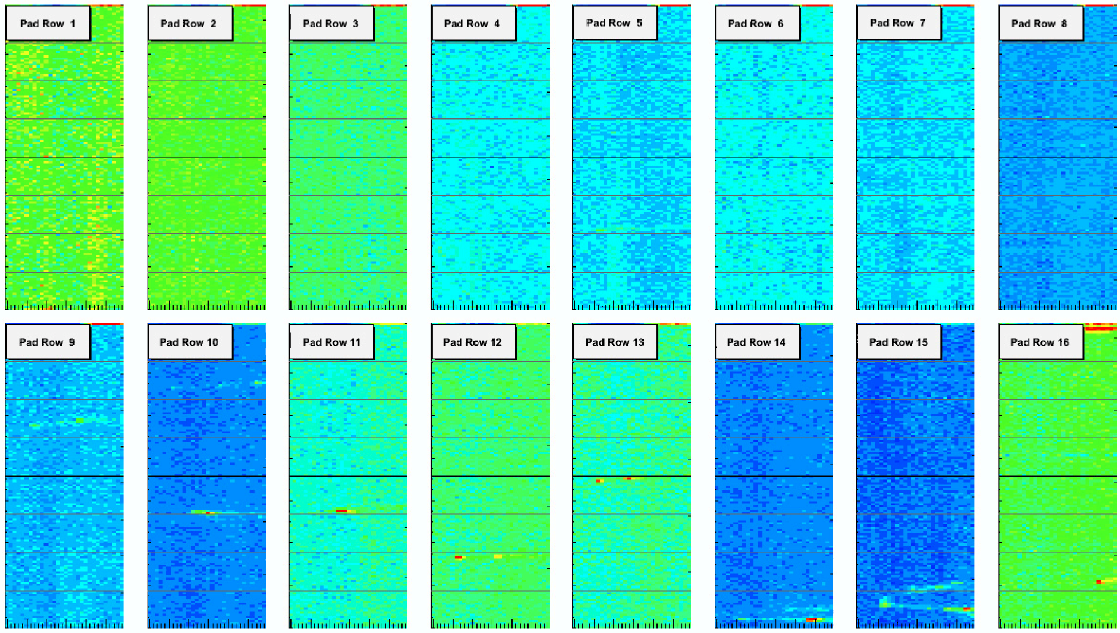

Figure 5.6: The first cosmic shower inside the supermodule.

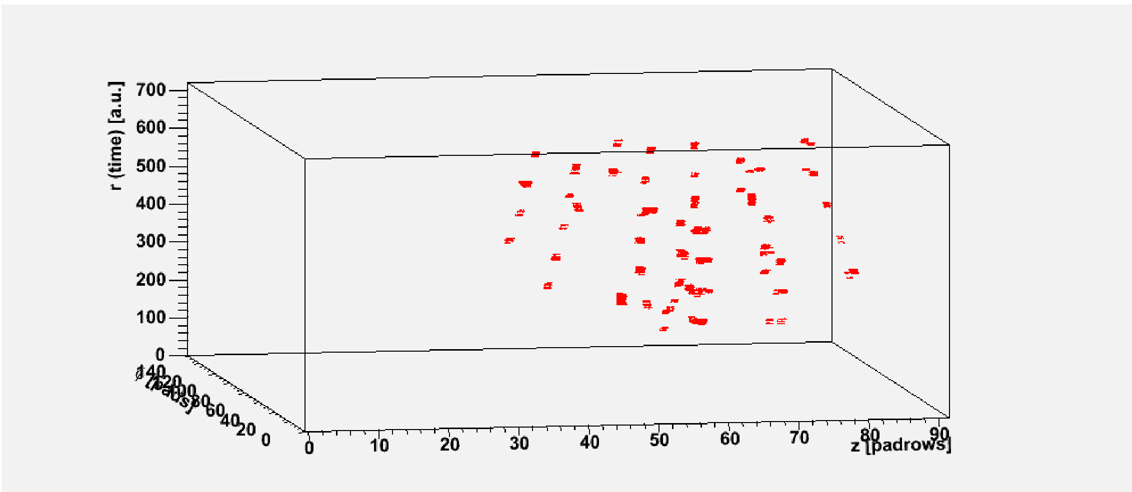

Figure 5.7: Display of tracks of a cosmic event inside the supermodule.

5.2.3 Re-Testing At CERN

The setup at CERN (Point 2, SXL2) is close to the setup in Heidelberg, it is sketched in Figure 5.11. The necessary computers are taken from Heidelberg to SXL2, to be able to perform the same tests as in Heidelberg. The cooling system, which also has to be transported from Heidleberg to CERN, is connected to the supermodule inlet and outlet to cool the MCMs. The cooling of the Wiener power supplies is done

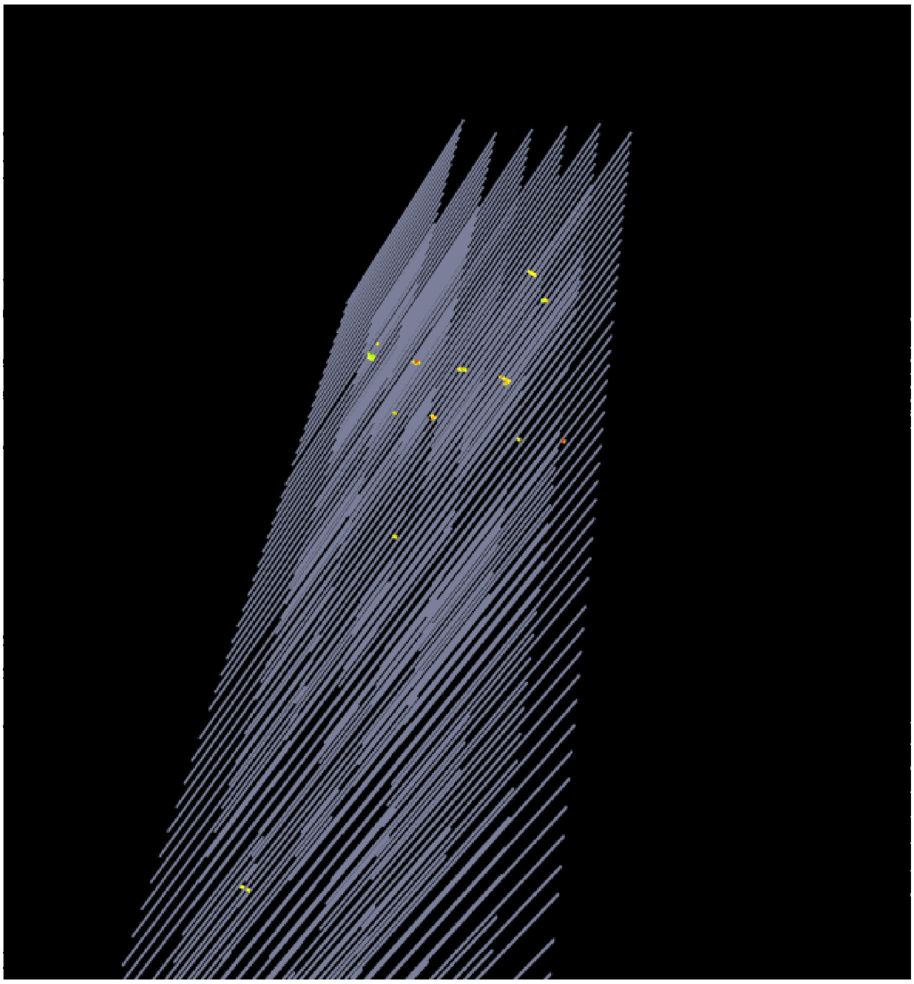

Figure 5.8: A cosmic event inside the supermodule seen with ALIROOT.

by a bypass of the laser cooling of the TPC. The needed electical currents are given from several power sockets in the Hall with one main socket. For testing, a computer setup consisting of all necessary PCs has been set up. First the powering of DCS boards has been checked. The next test checks the communication with the DCS boards. Now power can be given to the readout boards.
The tests continue with checking the configuration of the whole supermodule. Next steps are the stressing of the supermodule with several configurations of the electronics and the data taking of the supermodule, which is first noise taking. One example is shown in Figure 5.9, for testing purposes a half chamber merger in the chamber at layer 5 stack 1 is switched off.
With this tests also the stability of the power supplies and the cooling cycle is tested, this is done with the monitoring of the voltages, currents and the temperatures.

Gas Setup

To measure cosmic rays and recheck the tightness of the gas connections, a premixed Ar/CO_2 (82%/18%) gas is used. This leads to a change for the operational high voltage values, to achieve the nominal values of the drift velocity and of the gas amplification. The premixed gas has to be separated into three outlets, to flush two layers each. The connections for this are provided by copper tubes. The gas cycle on the supermodule side is done with stainless steel flexible pipes. Both is shown in Figure 5.12. To reduce

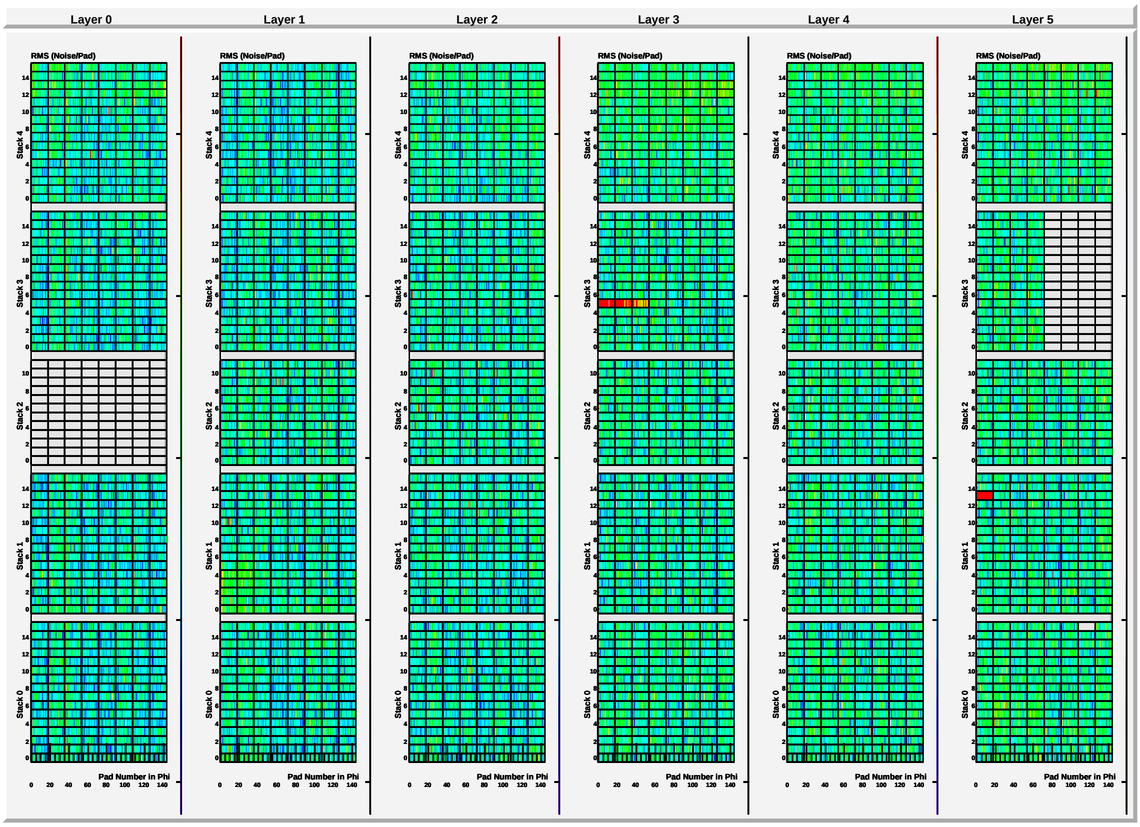

Figure 5.9: Example of a noise plot for all chambers in the supermodule taken at SXL2 at CERN.

the loss of gas and also the content of O_2 all gas clamps are closed very tight. Measurements of the O_2-concentration are done to evaluate the leak tightness of the setup. The time development of the O_2-concentration can be seen in Figure 5.10, since there was still gas inside the chambers the reaching of the plateau of about 9.5 ppm of the O_2-concentration could be reached. To flush the whole volume of the supermodule of about 1.51 m^3 takes nearly 24 h at a flow rate of above $120\frac{\mathrm{l}}{\mathrm{h}}$ per two layers. Since the calculation [CHI06] of the flow rate through the whole supermodule with a correction factor $k = 0.6 - 0.8 \approx 0.7$ between air and the gas mixture Ar/CO_2 (82%/18%) leads to

$$F = k \times 3 \times 120\frac{\mathrm{l}}{\mathrm{h}} = 0.7 \times 3 \times 120\frac{\mathrm{l}}{\mathrm{h}} = 252\frac{\mathrm{l}}{\mathrm{h}},$$

the calculation of the leak rate l shows:

$$l = 5\,\mathrm{bar} \times [O_2] \times F = 50 \times 10^{-6} \times 252\,\frac{\mathrm{l}}{\mathrm{h}} \approx 13\frac{\mathrm{mbar\,l}}{\mathrm{h}}.$$

HV And Cosmics

While gas is circulating through the chambers the high voltage is switched on. This is done for many hours to test the stability and to take cosmic events. The setup of the scintillators can be found in Figure 5.12, it is a little bit different compared to the setup in Heidelberg, since two scintillators are overlapping a little bit laying on a bar of the rotator frame and one is laying perpendicular to them on the ground at one side of the supermodule. Some impressions of the cosmic ray events in the supermodule at CERN are shown in Figure 5.13, using a tracklet finding tool, Figure 5.14, showing the distribution

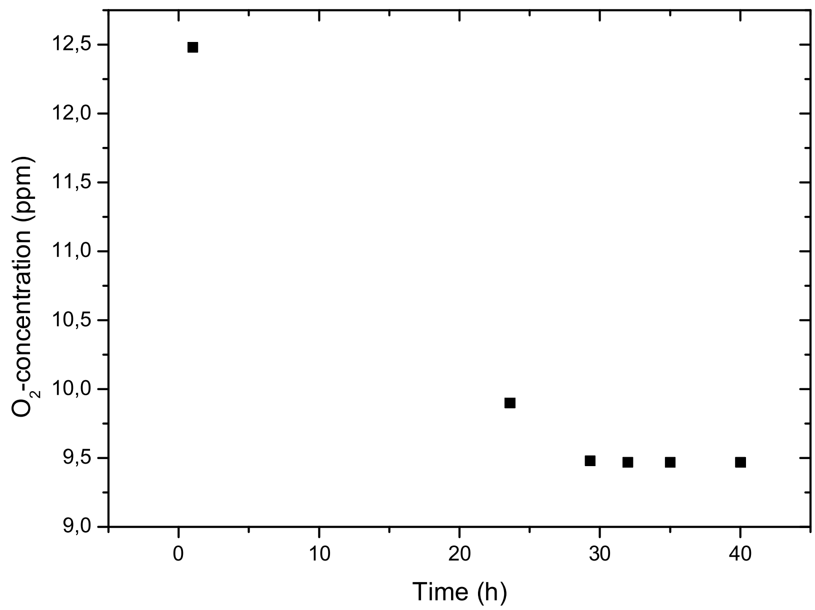

Figure 5.10: Results of the Measurement of the O_2 concentration at a constant temperature of 24.7 °C, starting the measurement after putting a new gas bottle.

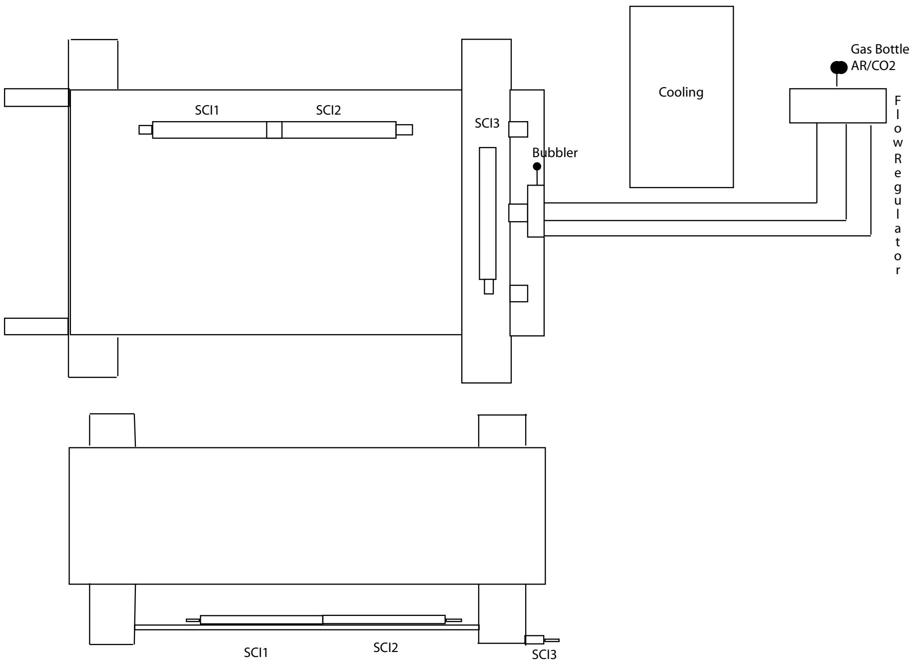

Figure 5.11: Scheme of the setup used in SXL2 to test the supermodule. The lower part shows the supermodule inside the rotator as seen from one side.

of signals and the average pulse height, for this distribution the 30 timebins of all ADC channels in the supermodule were used to analyse the cosmic shower to get the average pulse height as the amplitude in ADC counts, the distribution shows after a peak a plateau since no transition radiation was produced.

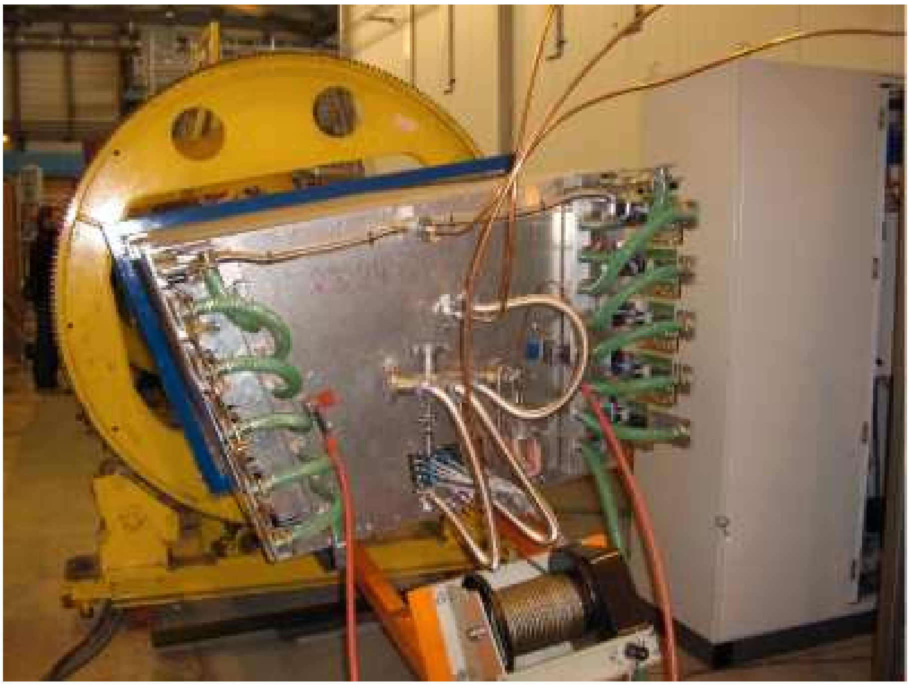

Figure 5.12: Supermodule at SXL2 seen from one side with connected gas, HV and ethernet, inside the rotator.

Figure 5.15, is produced using the monitoring tool which shows the tracklets in the stacks and the distribution of signals and the average pulse height for one event. Figure 5.16 shows a very intensive shower in the supermodule, this event was taken with the GTU and is visualized with ALIROOT.

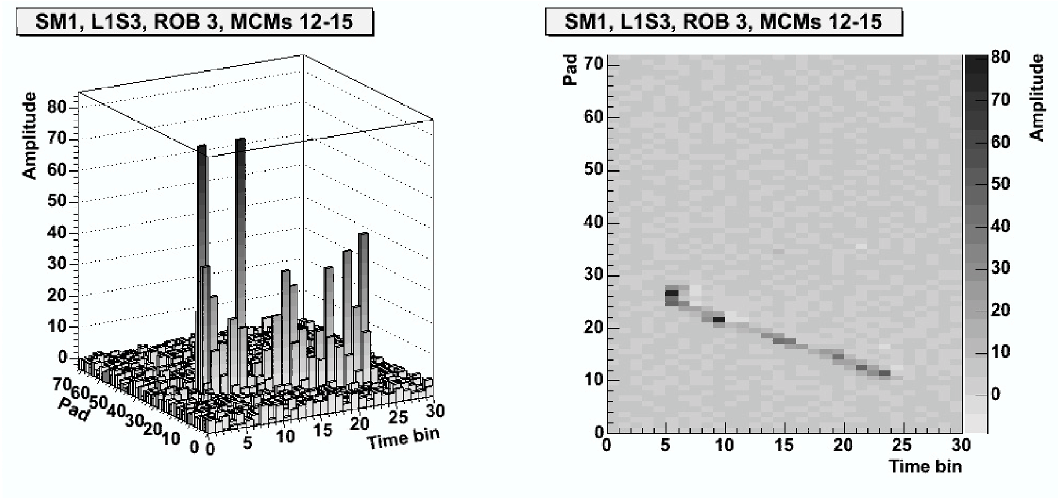

Figure 5.13: Close look to a cosmic event inside the supermodule taken at CERN. The found tracklet is easy to see.

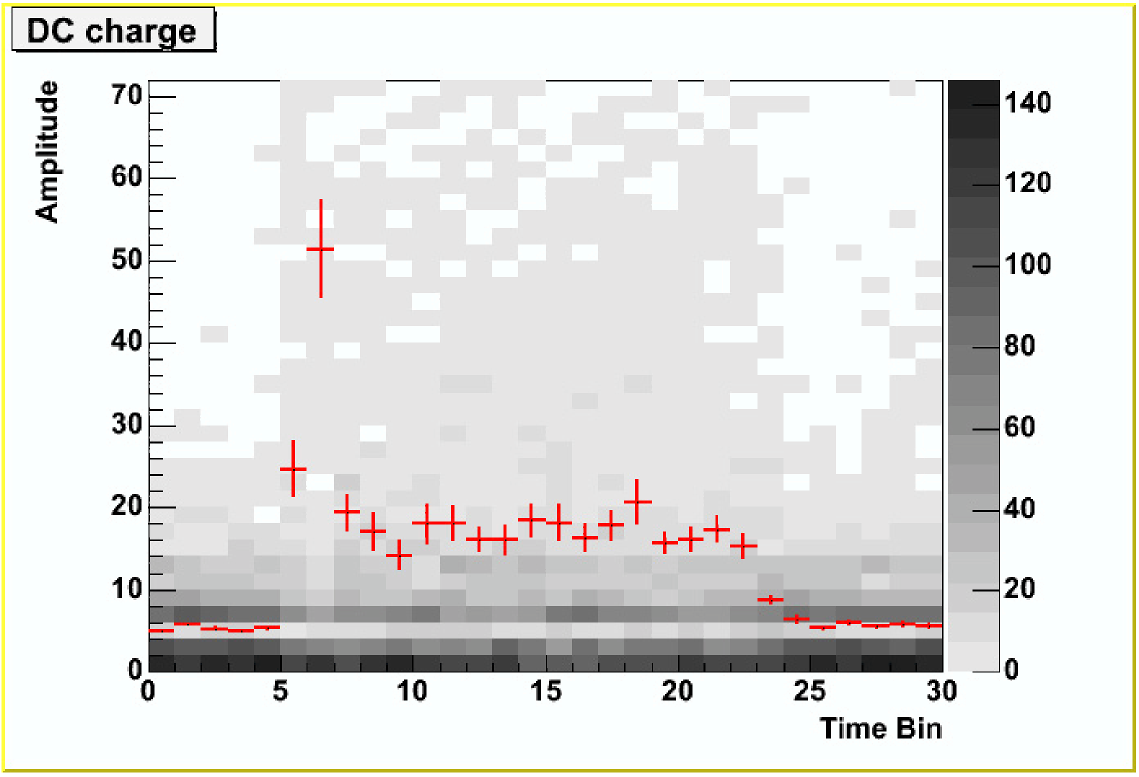

Figure 5.14: The distribution of signals and the average pulse height of all chambers for one cosmic event.

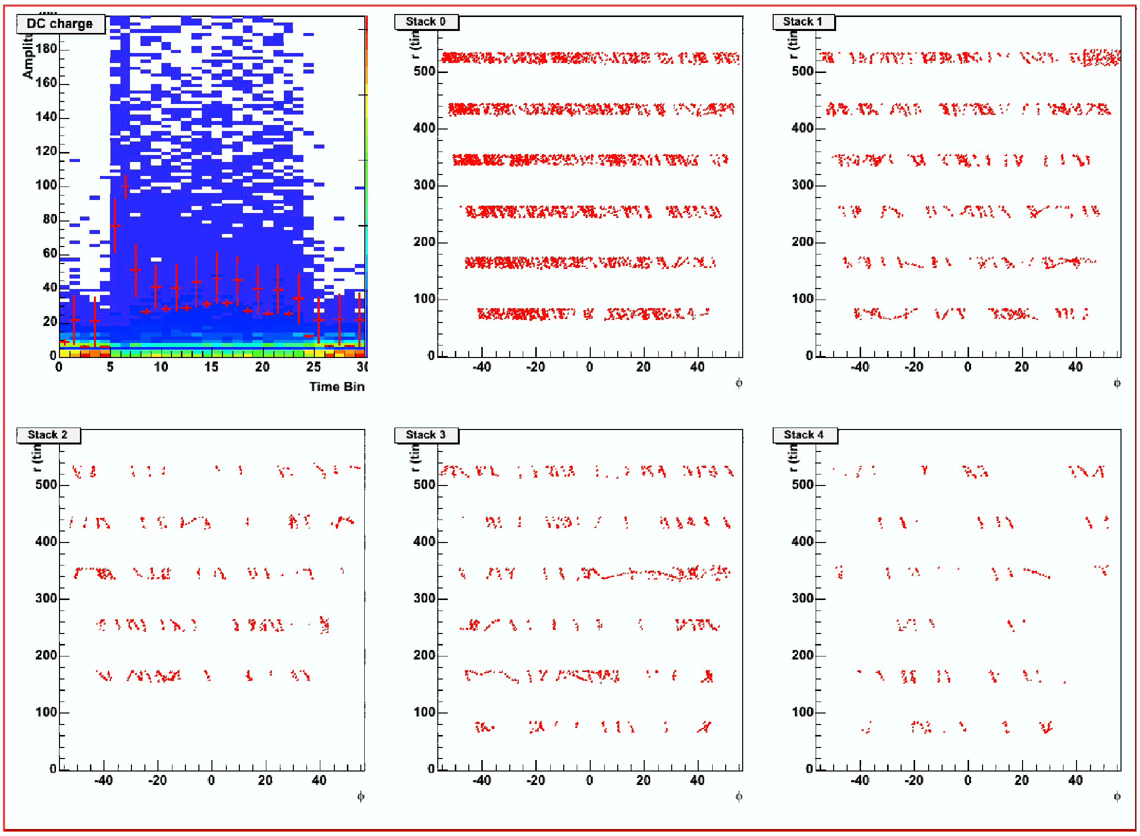

Figure 5.15: Monitor plot of a cosmic shower inside the supermodule taken at CERN.

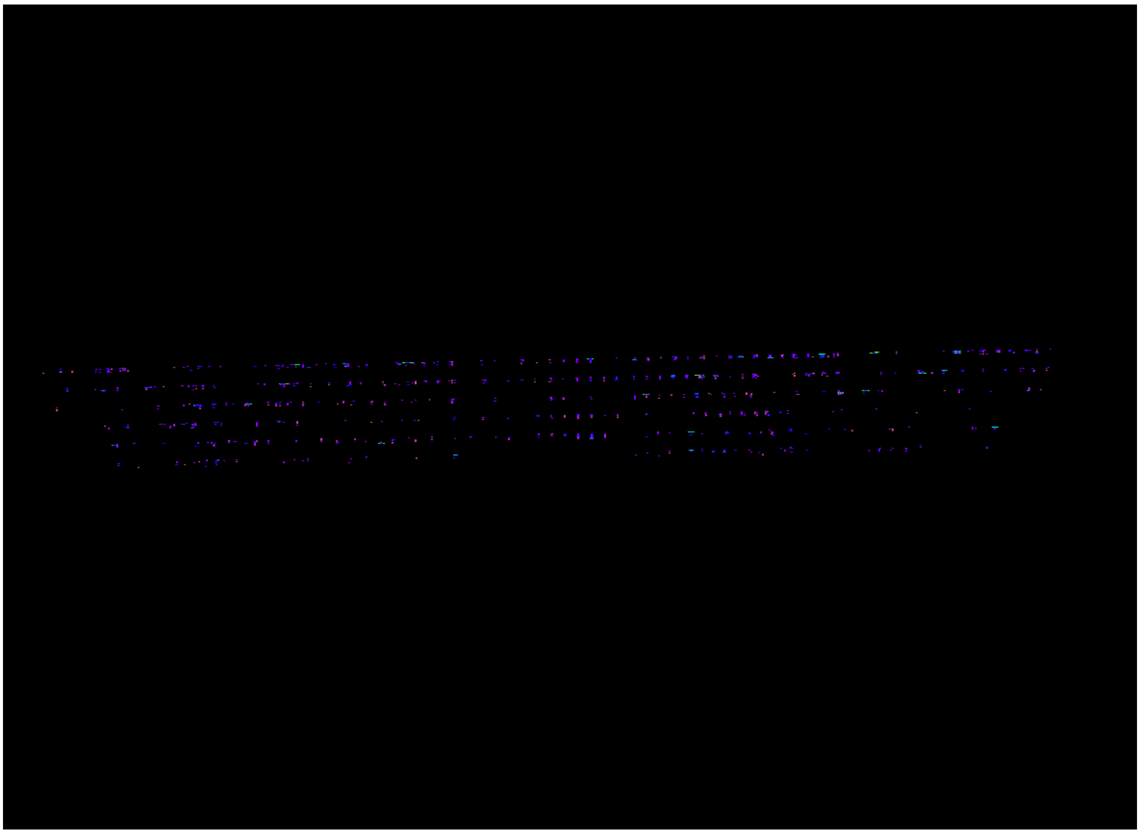

Figure 5.16: A cosmic ray event as seen by the supermodule taken with the GTU at CERN, visualized with ALI-ROOT.

Chapter 6

Outlook

The completed first supermodule of the ALICE TRD has been pulled into its place in sector 08 in the space frame at LHC, CERN. Seventeen more supermodules will be produced, tested and inserted into the space frame within the next two years. The construction of the next supermodule is presently taking place at the University of Münster, while the testing of the chambers is done at the University of Frankfurt.

In order to operate the first supermodule at the LHC the following steps are necessary:

- The commissioning of the first supermodule. The supermodule has to be checked in its final position and data of various kinds have to be taken to be able to calibrate and align the supermodule for the first pp collisions in autumn 2007.
  The first things for the commissioning have been done. The low voltage has been connected to the supermodule and is operable. Some noise events have been taken with DCS readout.
  The commisioning will go on when the GTU will be available to readout the whole supermodule and a cosmic trigger setup is in place.

- The programming of the software to configure, readout and analyse the data of one or more supermodules has to be continued. The finalisation of the PVSS projects to control the several services is nearly reached. The DCS framework is reaching a complete shape for TRD. The finite state machine, which controls the several PVSS projects is under development and will lead to the final control software for the Experiment Control System (ECS). Also the configuration through the database is under development and will soon reach a stage of applicability. The monitoring software MOOD is under development.

- The final services (LV, HV, gas) have to be installed, connected and tested. The layout of the low voltage connections for the first supermodule showed the necessity of a change of the last parts in the connection chain. Mainly the connections form the patch panel to the supermodule will be redesigned.

Appendix A

This appendix summarizes the noise data of the readout chambers of the first supermodule taken in Heidelberg before the mounting into the first supermodule. The data is presented in histograms which show the counts of different noise (rms) values of the ADC channels, for data with nf (red), p (blue) and pgt (lavender) configuration.

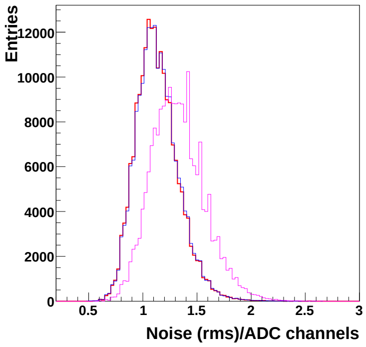

Figure A.1: Noise histogram for L0C0-015.

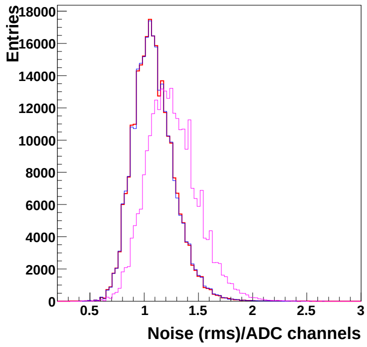

Figure A.2: Noise histogram for L0C1-001.

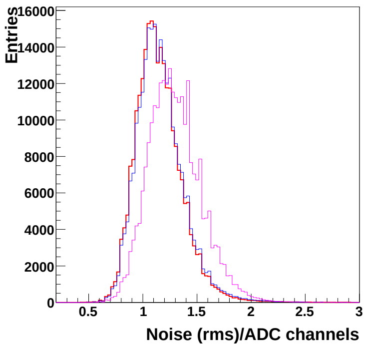

Figure A.3: Noise histogram for L0C1-002.

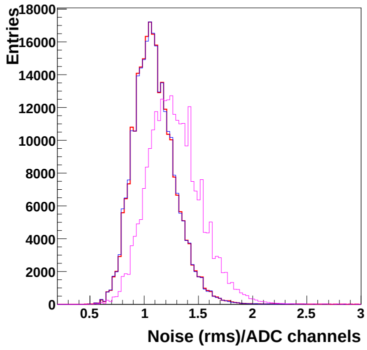

Figure A.4: Noise histogram for L0C1-003.

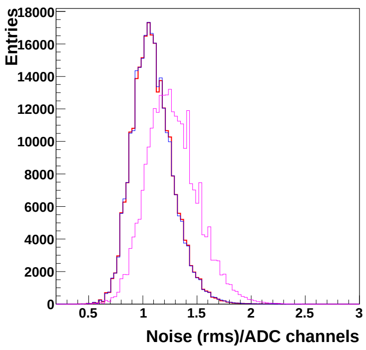

Figure A.5: Noise histogram for L0C1-004.

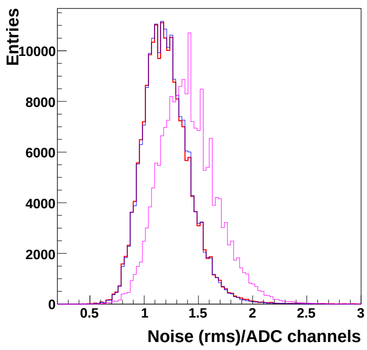

Figure A.6: Noise histogram for L1C0-008.

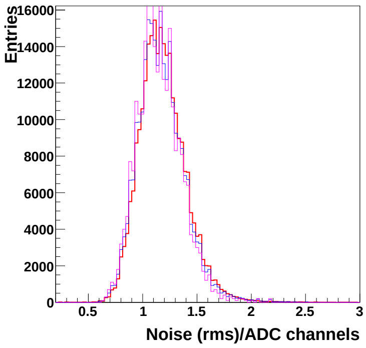

Figure A.7: Noise histogram for L1C1-002.

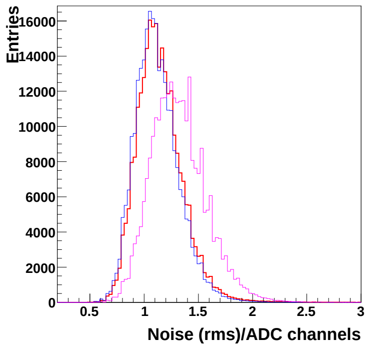

Figure A.8: Noise histogram for L1C1-011.

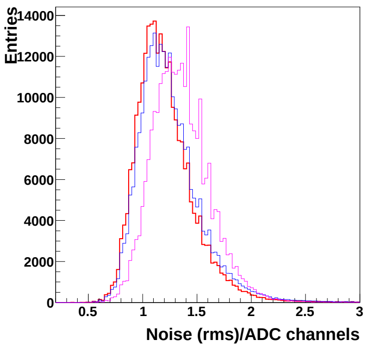

Figure A.9: Noise histogram for L1C1-019.

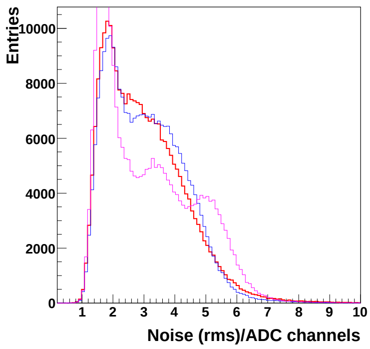

Figure A.10: Noise histogram for L1C1-020.

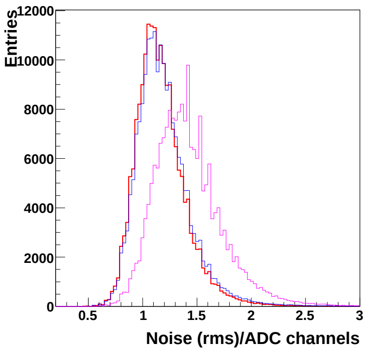

Figure A.11: Noise histogram for L2C0-005.

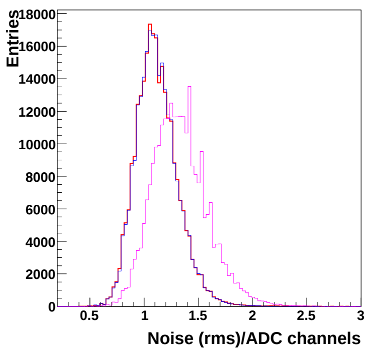

Figure A.12: Noise histogram for L2C1-001.

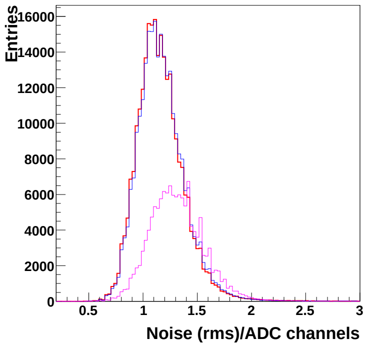

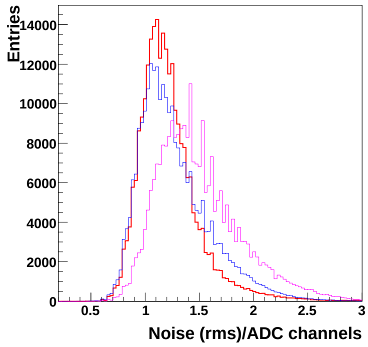

Figure A.13: Noise histogram for L2C1-003. **Figure A.14:** Noise histogram for L2C1-005.

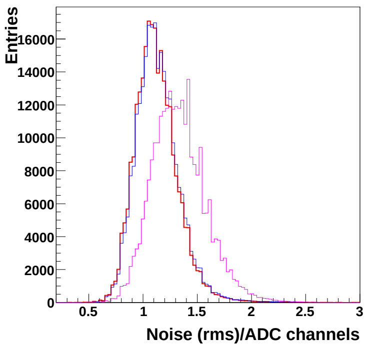

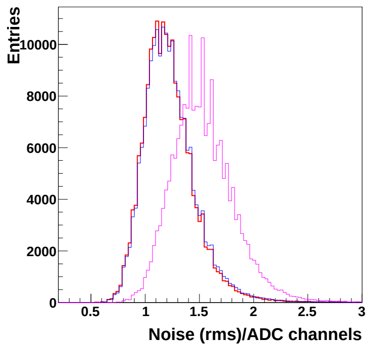

Figure A.15: Noise histogram for L2C1-018. **Figure A.16:** Noise histogram for L3C0-008.

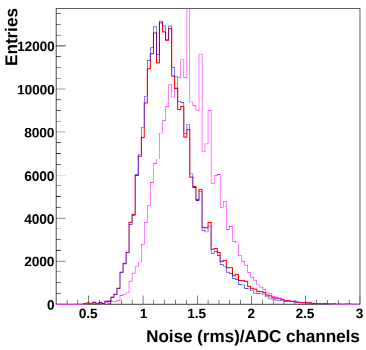

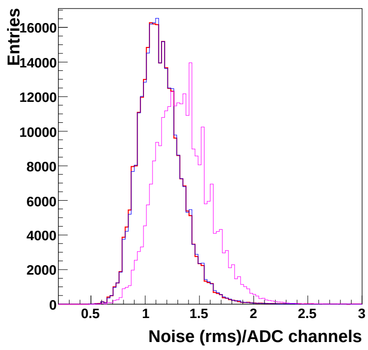

Figure A.17: Noise histogram for L3C1-017. **Figure A.18:** Noise histogram for L3C1-021.

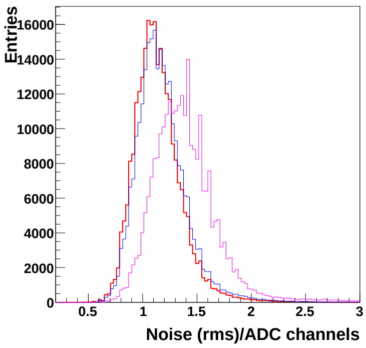

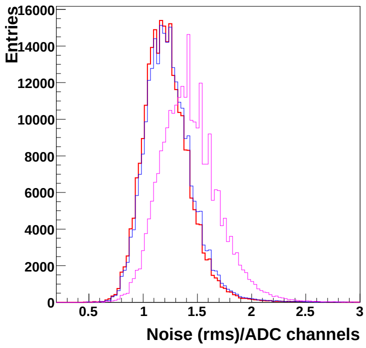

Figure A.19: Noise histogram for L3C1-023. **Figure A.20:** Noise histogram for L3C1-031.

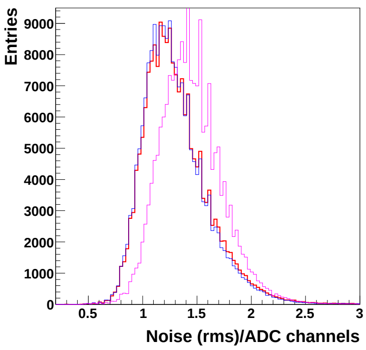

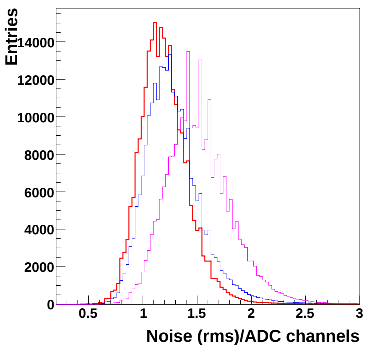

Figure A.21: Noise histogram for L4C0-018. **Figure A.22:** Noise histogram for L4C1-003.

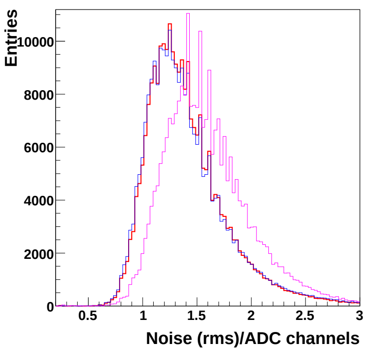

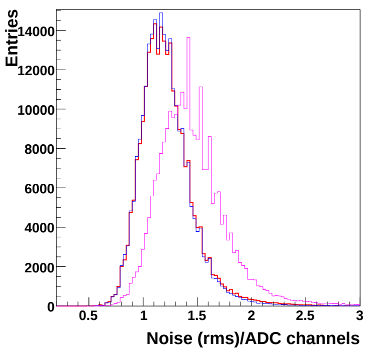

Figure A.23: Noise histogram for L4C1-004. **Figure A.24:** Noise histogram for L4C1-008.

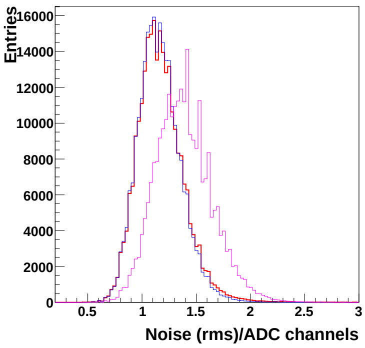

Figure A.25: Noise histogram for L4C1-011.

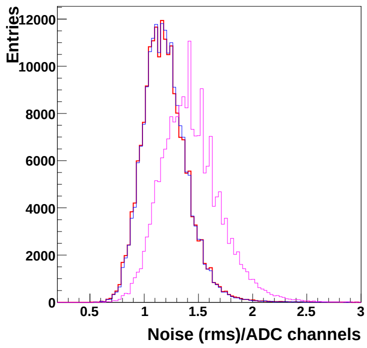

Figure A.26: Noise histogram for L5C0-001.

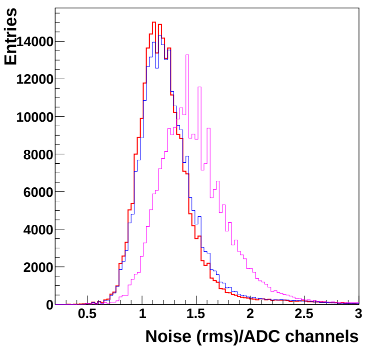

Figure A.27: Noise histogram for L5C1-003.

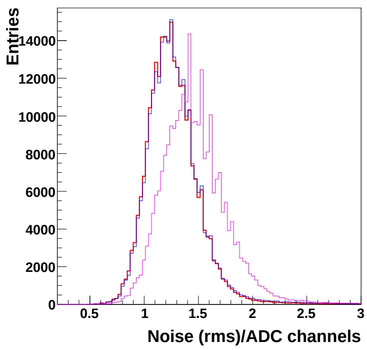

Figure A.28: Noise histogram for L5C1-004.

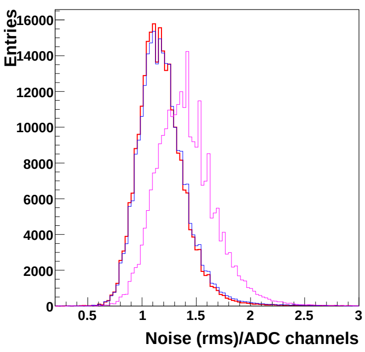

Figure A.29: Noise histogram for L5C1-034.

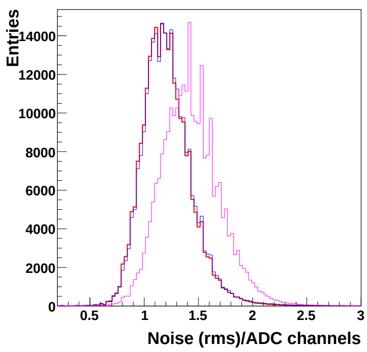

Figure A.30: Noise histogram for L5C1-035.

Bibliography

[ABS06] A. Andronic, P. Braun-Munzinger, J. Stachel, Nucl. Phys. A 772 (2006) 167

[AND06] A. Andronic et al., Nucl. Instr. Meth. A 558 (2006) 516

[ANG06] V. Angelov, Nucl. Instr. Meth. A 563 (2006) 317

[ANT06] V. Angelov et al., TRAP-Manual, Heidelberg (2006)

[AOK06] Y. Aoki et al., Phys. Lett. B 643 (2006) 46

[AON06] Y. Aoki et al., Nature 443 (2006) 675

[ART75] X. Artru et al., Phys. Rev. D 12 (1975) 1289

[ASH76] N. Ashcroft and N. Mermin, Solid State Physics, Harcourt College Publishers (1976)

[ATP95] ALICE Collaboration, Technical Proposal for A Large Ion Collider Experiment at the CERN LHC, CERN/LHCC/95-71, (1995)

[BAB06] S. Bablok et.al., Nucl. Instr. Meth. A 557 (2006) 631

[BAY95] G. Baym, Nucl. Phys. A 590 (1995) 233c

[BLÜ00] H. Blümler and K.H. Lampert, Physikalische Blätter 56 (2000) 39

[BUB04] M. Buballa, Habilitationsschrift (2004), Darmstadt

[BUS04] O. Busch, Nucl. Instr. Meth. A 522 (2004) 45

[CHE06] M. Cheng et al., Phys. Rev. D 47 (2006) 054507

[CHI06] C. Garabatos, private communication (2006)

[DEB23] P. Debye and E. Hückel, Phys. Z. 24 (1923) 185, 305

[DFS99] ALICE Collaboration, Dimuon Forward Spectrometer Technical Design Report, CERN/LHCC 1999-022, (1999)

[DOL93] B. Dolgoshein, Nucl. Instr. Meth. A 326 (1993) 434

[EMC06] ALICE Collaboration, Electromagnetic Calorimeter Addendum to the Technical Proposal, CERN/LHCC 2006-014, (2006)

[FOD04] Z. Fodor and S. Katz, J. High Ener. Phys. 04 (2004) 050

[FOR04] ALICE Collaboration, Forward Detectors: FMD, T0, V0 Technical Design Report, CERN/LHCC 2004-025, (2004)

[GAR04] R. Gareus, Diploma Thesis (2002), Heidelberg

[GIN46] V.L. Ginzburg and I.M. Frank, Zh. Eksp. Teor. Fiz. 16 (1946) 15

[GLE96] N. Glendenning, Compact Stars, Springer-Verlag (1996)

[GOJ59] P. Goldsmith and J.V. Jelley, Philosoph. Mag. 4 (1959) 836

[GUT06] M. Gutfleisch, Dissertation Thesis (2006), Heidelberg

[HMP98] ALICE Collaboration, HMPID Technical Design Report, CERN/LHCC 1998-019, (1998)

[ITS99] ALICE Collaboration, ITS Technical Design Report, CERN/LHCC 1999-012, (1999)

[JAC99] J. D. Jackson, Classical Electrodynamics, John Wiley and Sons (1999)

[LAT02] J. Letessier and J. Rafelski, Hadrons and Quark-Gluon Plasma, Cambridge University Press (2002)

[LIN04] V. Lindenstruth and L. Musa, Nucl. Inst. Meth. A 522 (2004) 33

[LIN06] V. Lindenstruth et al., GSI Scientific Report 2005, GSI Report 2006-1, (2006)

[LIP06] C. Lippmann, Proceedings of the SNIC Symposium, Stanfort, California - 3-6 April, 2006, http://www.slac.stanford.edu/econf/C0604032/papers/0043.pdf

[MAR00] M. Marder, Condensed Matter Physics, John Wiley and Sons (2000)

[PAR06] Particle Data Group, Review of Particle Physics, J. Phys. G: 33 (2006) 1

[PBM06] P. Braun-Munzinger and J. Wambach, Physik Journal 5 (2006) 41

[PBM07] P. Braun-Munzinger, arXiv.org/nucl-th/0701093 (2007)

[PER00] D. H. Perkins, High Energy Physics, Cambrige University Press (2000)

[PHO99] ALICE Collaboration, PHOS Technical Design Report, CERN/LHCC 1999-004, (1999)

[PMD99] ALICE Collaboration, PMD Technical Design Report, CERN/LHCC 1999-032, (1999)

[POV06] B. Povh et al., Teilchen und Kerne, Springer-Verlag (2006)

[PPR04] ALICE Collaboration, ALICE: Physics Performance Report, Volume I, J. Phys G: Nucl. Part. Phys. 30 (2004) 1517

[PPR06] ALICE Collaboration, ALICE: Physics Performance Report, Volume II, J. Phys G: Nucl. Part. Phys. 32 (2006) 1295

[REN07] R. Renfordt, private communication (2007)

[RET07] F. Rettig, Diploma Thesis (2007), Heidelberg

[RUS06] I. Rusanov and J. Stachel, GSI Scientific Report 2005, GSI Report 2006-1, (2006) 287

[SOL04] H. K. Soltveit et al., GSI Scientific Report 2003, GSI Report 2003-1, (2004) 244

[SOL07] H. K. Soltveit, private communication (2007)

[STE07] J. Steckert, Master Thesis (2007), Heidelberg

[TDR04] ALICE Collaboration, Trigger Data Acqusition, High Level Trigger, Control System Technical Design Report, CERN/LHCC 2003-062, (2004)

[TOF02] ALICE Collaboration, TOF Addendum to the Technical Design Report, CERN/LHCC 2002-016, (2004)

[TPC00] ALICE Collaboration, TPC Technical Design Report, CER/LHCC 2000-001, (2000)

[TRD99] ALICE Collaboration, TRD Technical Design Report, CERN/LHCC 2001-021, (2001)

[UA183] UA1 Collab. G. Arnison et al.: Phys. Lett. 126B, 398 (1983)

[UA283] UA2 Collab. P. Bagnaia et al.: Phys. Lett. 129B, 130 (1983)

[UNS99] H. Unsöld and K.H. Baschek, Der neue Kosmos, Springer-Verlag (1999)

[VÖL00] H. Völk, Physikalische Blätter 56 (2000) 35

[WER04] V. Werth, Diploma Thesis (2004), Darmstadt

[WON94] C.-Y. Wong, Introduction to High-Energy Heavy-Ion Collisions, World Scientific Publishing (1994)

[YAG05] K. Yagi, T. Hatsuda and Y. Miake, Quark-Gluon Plasma, Cambridge University Press (2005)

[ZDC99] ALICE Collaboration, ZDC Technical Design Report, CERN/LHCC 1999-005, (1999) A.Andronic, P.Braun-Munzinger, J.Stachel

ACKNOWLEDGMENTS

I would like to thank Prof. Dr. Peter Braun-Munzinger who provided me with such a nice topic. Just by one question!

I would like to especially acknowledge Dr. Anton Andronic who helped me with all kinds of problems. The same i have to say for Dr. Christian Lippmann. He helped me in various situations, especially at CERN.

My thanks go to the Heidelberg colleagues who helped me to understand the problems i encountered. Mainly Dr. Ken Oyama, Dr. Kai Schweda, Dipl.-Phys. David Emschermann, Dr. Clemens Adler, Dr. Ivan Rusanov and Dr. Thomas Dietel (who is no real Heidelbergian but close).

I also would like to thank the rest of the Heidelbergians for the nice enviroment they produced. Especially Jens Steckert, Min Jung Kweon, Felix Rettig, Dr. Georgios Tsiledakis, Dr. Bernd Windelband and his crew.

I would like to express my gratitude to Dr. Venelin Angelov who helped me to understand the TRAP, and Dr. Hans Kristian Soltveit who did the same for the PASA.

Many thanks i owe as well to Dr. Jose 'Chilo' Garabatos who introduced me into the gas business of the TRD.

I am also thankful to the guys and girls from GSI who integrated me so nicely after a long time far away! I also would like to thank our secretary Sandra Schecker, who helped me with all the bureaucratic parts connected to my work.

For reading this thesis to reduce mistakes of certain kinds i have to thank Dr. Kai Schweda, Dr. Christian Lippmann, Dr. Anton Andronic and Caroline Kühnle.

This work has been supported by GSI which carried the costs of my travels.

Last but not least i would like to thank my parents who provided me the chance to this. And finally i have to thank my fiancée Caroline for her trust and for believing in me.

Erklärung zur Diplomarbeit

(gem 19 Abs. 6 DPO/AT)

Hiermit versichere ich, die vorliegende Diplomarbeit ohne Hilfe Dritter nur mit den angegebenen Quellen und Hilfsmitteln angefertigt zu haben. Alle Stellen, die aus den Quellen entnommen wurden, sind als solche kenntlich gemacht worden. Diese Arbeit hat in gleicher Form noch keiner Prüfungsbehörde vorgelegen.

Babenhausen, 30. April 2007

(Benjamin Dönigus)